Correspondence to:

B. Kaifler,
bernd.kaifler@dlr.de

Mountain Wave Momentum Flux Estimates From Airborne Lidar Measurements in the Middle Atmosphere Above the Southern Andes

Bernd Kaifler[1] ，**Natalie Kaifler[1]** ，**Markus Rapp[1,2]** ，**and Andreas Dörnbrack[1]**

[1]Institut für Physik der Atmosphäre, Deutsches Zentrum für Luft- und Raumfahrt, Wessling, Germany, [2]Meteorologisches Institut, Ludwig-Maximilians-Universität München, Munich, Germany

Abstract Cross-mountain flow over the Southern Andes and strong zonal winds extending higher up in the atmosphere allowed for mountain waves to penetrate into the mesosphere on 11/12 September 2019 during the Southern Hemisphere Transport, Dynamics, and Chemistry–Gravity Waves (SOUTHTRAC-GW) campaign. The middle atmosphere responses above and in the lee of the mountain ridge were observed by the Airborne Lidar for Middle Atmosphere Research (ALIMA) onboard the German High-Altitude and Long-Range research aircraft (HALO), which provided temperature measurements with both high horizontal ($\sim$10 km) and high vertical (1.5 km) resolution. The observations reveal a complex wave field with multiple superimposed wave packets with horizontal scales λ_h ranging from $\sim$33 to 395 km. This paper employs spectral analysis of observational data and results of Fourier ray modeling to decompose the wave field and analyze the scales and properties of gravity wave packets. Profiles of the vertical flux of horizontal mountain wave momentum reveal contributions of each wave packet to the total momentum flux and gravity wave drag. The derived momentum flux spectrum suggests a spectral response of the form λ_h^x with the exponent in the range -1.0 to -1.2 and peak momentum flux occurring at approximately $\lambda_h = 45$ km. Results show that >80 % of the total mountain wave momentum flux is carried by waves with $\lambda_h < 100$ km.

Plain Language Summary Mountain waves are oscillations in the atmosphere that result from disturbances in the horizontal air flow caused by mountains. In this study we use remote-sensing data collected by the Airborne Lidar for Middle Atmosphere Research (ALIMA) onboard the HALO research aircraft to investigate the properties of waves generated by the Southern Andes. The lidar provided temperature measurements with both high vertical (1.5 km) and high horizontal ($\sim$10 km) resolution along the flight track of the aircraft in the altitude range 20–70 km. We analyze the horizontal and vertical scales of observed mountain waves, compute energy density and momentum flux profiles, and derive energy and momentum flux spectra. Our results show that >80 % of the total mountain wave momentum flux is carried by waves with small horizontal scales that are typically not resolved in numerical weather prediction models and climate models. This finding may be important for correcting biases in models.

1. Introduction

The southern part of South America is known as the worlds strongest gravity wave hotspot in the stratosphere based on satellite measurements (e.g., Eckermann & Preusse, 1999; Ern et al., 2004; Hendricks et al., 2014; Hoffmann et al., 2013, 2016). In this region, westerly winds excite large-amplitude mountain waves above the approximately north-to-south oriented Andes mountain range. From a climatological perspective, the tropospheric jet and the polar night jet both provide suitable conditions for propagation of these waves into the mesosphere during austral winter.

Lidar temperature measurements at two sites in the vicinity of the mountains show very large wave amplitudes in the stratosphere and in the mesosphere-lower thermosphere (MLT) region (Huang et al., 2017, 2021; N. Kaifler et al., 2020; Reichert et al., 2021). Evidence for the occurrence of mountain waves in the MLT region above the Andes also comes from OH imager studies (Pautet et al., 2021; S. Smith et al., 2009). At altitudes where these waves break, large gravity wave drag arises, with the potential to generate secondary waves that propagate further up (de Wit et al., 2017; Kogure et al., 2020). Radars provide information on mean winds, waves and tides in the upper mesosphere (e.g., Hindley et al., 2022; Stober et al., 2021), while most stratospheric observations above the Southern Andes come from satellite-based instruments.

The latter tend to underestimate the vertical flux of horizontal gravity wave momentum due to limitations in resolving smaller-scale waves (Hindley et al., 2015; Preusse et al., 2009). However, there is evidence that these smaller-scale waves are of high importance for atmospheric dynamics. For example, R. B. Smith et al. (2016) and Fritts et al. (2021) show that most of the momentum flux carried by mountain waves is due to waves with horizontal wavelengths $\lambda_h < 100$ km, which is in line with theoretical arguments put forward as early as in the 1980s (e.g., Fritts, 1984). These results obviously bring up the question how much of the total momentum flux is missed by the satellite observations. The answer to this question is particularly relevant regarding the potential role of mountain waves, that are generated by the airflow across the Southern Andes and refracted into the core of the polar night jet (e.g., Gupta, Sheshadri, et al., 2024; Sato et al., 2012), in contributing to the so-called gravity wave belt at 60°S. At the same time, global circulation models continue to underestimate the gravity wave drag at these latitudes, highlighting our lack of understanding of relevant dynamic processes (e.g., Garcia et al., 2017; Gupta, Reichert, et al., 2024; McLandress et al., 2012; Plougonven et al., 2020). There is therefore a pressing need to obtain high-resolution measurements that cover the smaller scales which are typically not resolved in satellite-based observations, and to combine these measurements with high-resolution numerical modeling.

During the international Southern Hemisphere Transport, Dynamics and Chemistry—Gravity Wave (SOUTH-TRAC-GW) campaign, coordinated observations in the troposphere, stratosphere, and mesosphere using multiple instruments on various platforms were carried out. The aim of this campaign was to investigate the excitation of mountain gravity waves over the Southern Andes and/or Antarctic Peninsula, and to study how these waves propagate into the polar night jet (see Table 1 in Rapp et al. (2021) for specific campaign goals). The primary platform was the German High-Altitude and Long-Range research aircraft (HALO), which carried a set of active and passive remote sensing instruments as well as in situ instruments. The main payloads dedicated to observations of waves were the Airborne Lidar for Middle Atmosphere Research (ALIMA), the Gimbaled Limb Observer for Radiance Imaging of the Atmosphere (GLORIA), and the Basic HALO Measurement and Sensor System (BAHAMAS) (Rapp et al., 2021, and references therein). ALIMA provided temperature profiles above the aircraft, while the side-looking GLORIA instrument measured temperature and trace gas concentrations from flight level down to the cloud top. BAHAMAS provided high-resolution in situ measurements of temperature, pressure, wind speed and wind direction.

In this work, we present and analyze data acquired by the ALIMA instrument, which was deployed for the first time during the SOUTHTRAC campaign. ALIMA measured vertically resolved profiles of temperature from 20 to about 70 km altitude. From these temperature curtains along the flight track, signatures of gravity waves are retrieved with a vertical resolution of 1.5 km and a horizontal resolution of 10–15 km. The horizontal resolution is about a factor 3 coarser compared to airborne sodium lidar data shown in Bossert et al. (2018), but unlike the Bossert et al. (2018) study which is limited to the upper mesosphere, our measurements cover most of the stratosphere and mesosphere. We present a case study of prominent mountain waves that propagated into the mesosphere and were observed during research flight ST08 on the night of 11/12 September 2019. We focus on the two cross-mountain legs of ST08 directly above the Southern Andes where the strongest gravity wave amplitudes were observed. We address the following questions: (a) What are the dominant vertical and horizontal wavelengths, amplitudes and potential energy densities of the observed mountain waves? (b) How much horizontal momentum do gravity waves of different horizontal scales carry? (c) How much do gravity waves from the Southern Andes hot spot contribute to the zonal mean gravity wave drag?

Section 2 describes the meteorological conditions during flight ST08, the ALIMA temperature measurements, and the data reduction steps we took in order to analyze the complex, multi-scale gravity wave field and derive gravity wave properties. The results are shown in Section 3, the implications regarding the above questions are discussed in Section 4, and our summary and conclusions are given in Section 5.

2. Data and Methods

2.1. Meteorological Conditions on 11/12 September 2019

Meteorological forecasts indicated favorable conditions for both mountain wave excitation and propagation into the stratosphere and mesosphere for 11/12 September 2019. Strong near-surface winds turning from the northwest to south-west on 11 September 2019 (see Figure 13 in Dörnbrack et al., 2020) provided the necessary forcing. The low-level forcing ceased during the day and the reported wave activity over the Andes near El Calafate became weaker during the night of 11/12 September 2019 (Dörnbrack et al., 2020). The horizontal winds
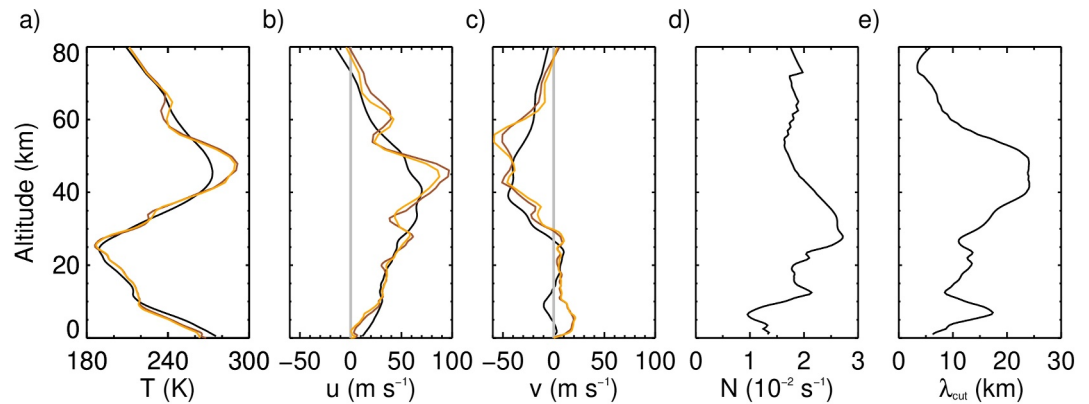
Figure 1. Area-averaged (see trapezoidal box in Figure 2) ECMWF IFS T21 profiles representative of the background conditions on 11 September 2019 12:00 UT (black lines) and two snapshots above the mountains (for locations see Figure 2) representative of conditions during the flight on 11 September 2019 23:55 UT (brown; leg 1) and 12 September 2019 01:00 UT (yellow; leg 2): (a) temperature, (b) zonal wind component, (c) meridional wind component, (d) Brunt-Väisälä frequency and (e) cut-off wavelength.

as analyzed by the European Center for Medium-Range Weather Forecasts Integrated Forecasting System (ECMWF IFS) revealed a west-northwesterly airflow at about 20 km altitude that turned to northwesterly flow aloft (see Figures 4 and 13 in Rapp et al., 2021). This change in wind direction was caused by the ongoing sudden stratospheric warming that displaced and twisted the stratospheric polar vortex (Lim et al., 2021). The two mountain crossings of research flight ST08 were designed to run parallel to the airflow in the upper stratosphere and follow the core of the polar night jet.

Figure 1 shows the ECMWF IFS area-averaged vertical profiles of temperature T, zonal and meridional wind components u and v, and buoyancy frequency $N = \sqrt{\frac{g}{\Theta}\frac{\partial\Theta}{\partial z}}$. The location and size of the box over which the quantities were averaged is shown in Figure 2. The ECMWF IFS data were spectrally truncated at T21 in order to reduce the effect of gravity waves. For reference, we also show two snapshots (colored lines) for two locations above the mountains and times when the aircraft passed these locations. To derive these profiles, the ECMWF IFS data were interpolated in space and time along the flight track. The temperature decreased in the troposphere and stratosphere to a minimum of about 190 K at about 25 km, where polar stratospheric clouds were observed on this day (Dörnbrack et al., 2020). The stratopause was located at ~45 km altitude. The zonal wind was strongest within the core of the polar night jet at ~40 km altitude and the wind direction reversed at ~70 km, resulting in a critical level for stationary mountain waves. From the approximated Scorer parameter $l = \sqrt{N^2 U^{-2}}$ using the horizontal wind $U = \sqrt{u^2 + v^2}$ we calculated the cut-off wavelength $\lambda_{cut} = 2\pi l^{-1}$ separating propagating and evanescent waves. The result shown in Figure 1e reveals that mountain waves with $\lambda_h > 17$ km were able to propagate into the lower stratosphere. Mountain waves with λ_h between 17 and 24 km encountered a turning level at about 35–40 km altitude, while waves with larger λ_h could propagate into the mesosphere.

2.2. Flight Track of Research Flight ST08

During the SOUTHTRAC-GW campaign, the HALO aircraft was based in Río Grande at the east coast of Tierra del Fuego island, Argentina (53.78°S, 67.78°W). The location was an ideal choice not only for logistical reasons, but also for being at the center of the area to be sampled; the area encompassing the high peaks of the Andes mountain range, the Drake passage where the polar vortex edge could be probed, and the Antarctic Peninsula as an additional strong source of mountain waves. Figure 2 shows the orography with the flight track marked by black solid lines. The underlying data are from the

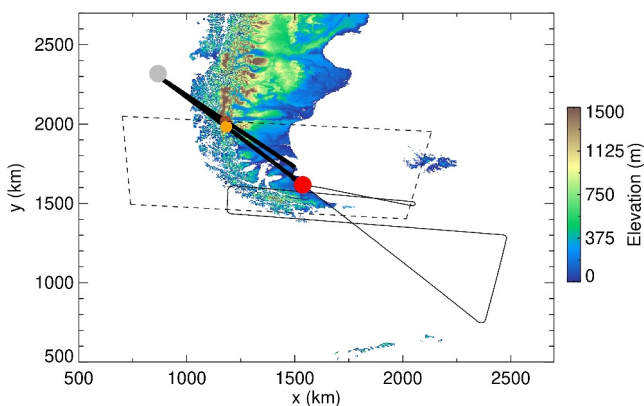**Figure 2.** Orography of South America with the HALO flight track shown as black solid line and legs 1 and 2 highlighted in bold. The red dot marks Río Grande, the gray dot the turning point over the Pacific, and the brown and orange dots the locations of the colored ECMWF IFS profiles shown in Figure 1. The domain of the averaged ECMWF IFS profiles in Figure 1 is indicated as a dashed trapezoidal box.
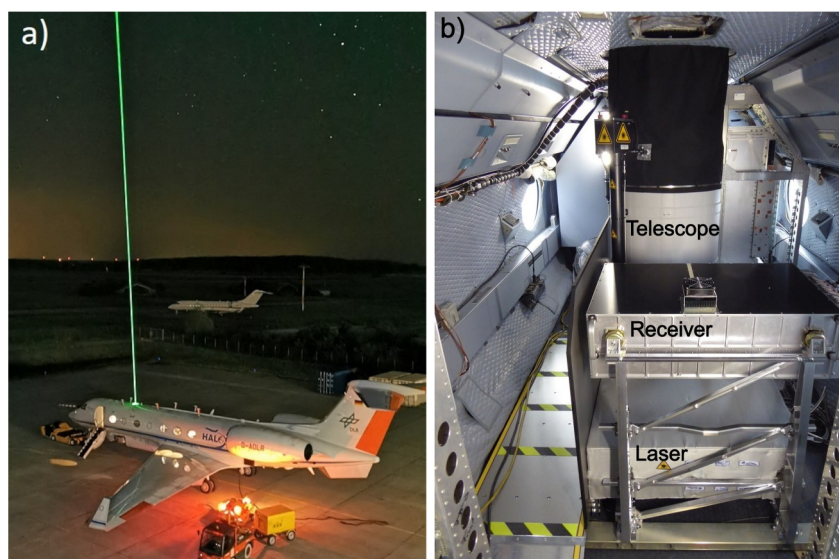
Figure 3. (a) HALO with the ALIMA laser beam during tests in Oberpfaffenhofen, Germany on 22 August 2019. Photo: C. Michael Volk, University of Wuppertal. (b) The ALIMA instrument inside the aircraft cabin. Photo: Bernd Kaifler.

Advanced Spaceborne Thermal Emission and Reflection Radiometer (ASTER) elevation model (Abrams et al., 2020) downsampled to 4 km × 4 km resolution. Taking off at Río Grande at 23:10 UT on 11 September 2019, HALO turned to the northwest and crossed mountain peaks of ~1,500 m elevation before passing the west coast, and continued in this direction for a further 170 km out over the Pacific. At 0:28 UT, at the location 47.65°S and 77.61°W, HALO reversed course, taking a slightly larger southerly heading. HALO crossed over Río Grande and continued on this course for another ~1,000 km, then turned north and finally west when the aircraft reached the latitude of the southern tip of South America. Following a racetrack pattern, HALO crossed the southern tip twice before again heading out over the ocean and returning to Río Grande.

The strongest mountain wave responses were observed above the larger mountain peaks which HALO crossed twice in the first half of the flight. These two mountain crossings are the foci of our study. We define leg 1 as an 836 km long segment heading northwest between 23:20 UT and 00:26 UT. The highest peak of 1,574 m was crossed at 23:57 UT. Leg 2 is slightly longer (916 km) and covers the period 00:30 UT to 01:31 UT with heading southeast. The distance was calculated in steps of 10 s along a great circle. The azimuth angles of the legs are 137.9° (leg 1) and 134.3° (leg 2) clockwise from north. The short excursion to the north right after take-off that resulted in slightly different headings for the two legs was not planned and necessitated by the departure corridor of the airport.

2.3. ALIMA Measurements

The ALIMA instrument is a monostatic Rayleigh lidar which utilizes Rayleigh scattering of emitted laser light to measure atmospheric backscatter profiles. In the absence of aerosols, which is typically the case in the upper stratosphere and mesosphere, the backscatter profiles are proportional to air density. The measured profiles can then be converted to temperature profiles by hydrostatic integration.

The instrument setup is similar to the ground-based CORAL instrument described in B. Kaifler and Kaifler (2021) but with modifications to allow for operation of the instrument onboard an aircraft. ALIMA uses a diode-pumped and frequency-doubled Nd:YAG laser with 12.5 W mean optical output power at 532 nm wavelength and 100 Hz pulse repetition frequency. The expanded laser beam is transmitted through a window in the upper fuselage of the aircraft in coaxial configuration with the 0.48 m diameter receiving telescope (see Figure 3). In the receiver, three cascaded detection channels are used to detect and timestamp backscattered laser photons with 800 ps resolution, covering most of the middle atmosphere from about 5 km above the flight level to approximately 90 km altitude (in this work profiles are cut at ~70 km). The timestamps were converted to photon count profiles with 100 m vertical resolution and 1 min time resolution in post-processing. Changes in the pointing of the laser beam as a
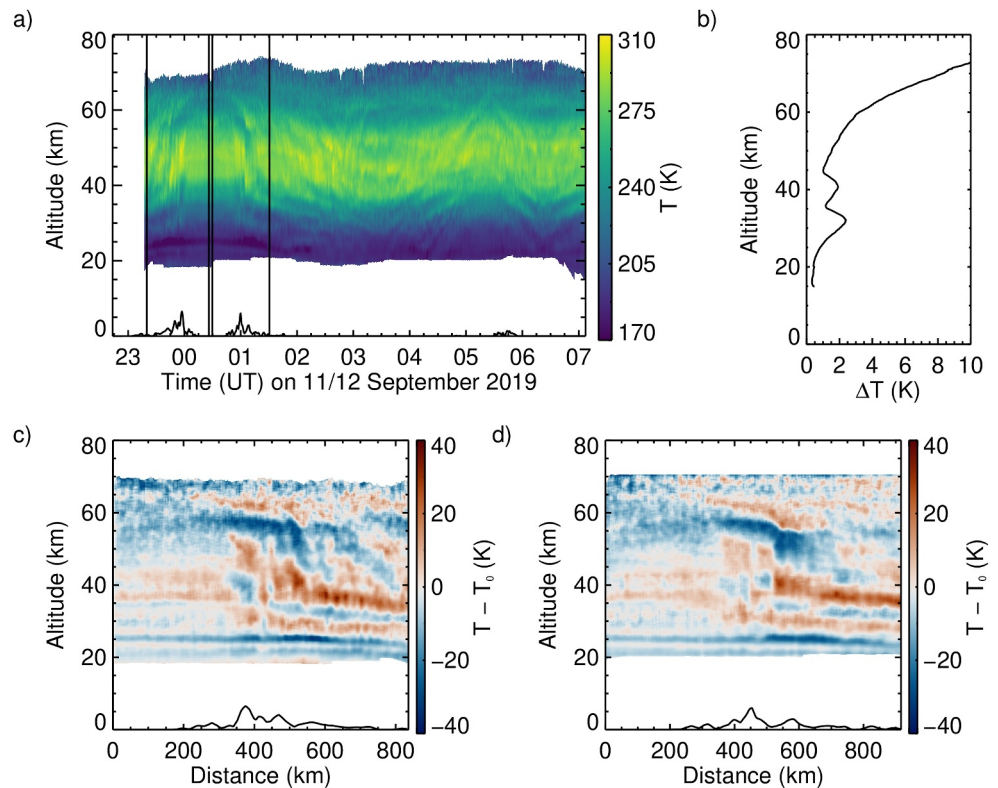
Figure 4. (a) ALIMA temperature measurements at 1 min × 1,500 m resolution. The vertical black lines indicate start and end points of legs 1 and 2. (b) The flight mean average of the corresponding measurement uncertainties. (c, d) ALIMA temperature perturbations for legs 1 and 2 interpolated on a regular distance grid. The curtains are oriented such that the turning point above the Pacific is at 0 km distance. The orography as shown by the black curve in the lower part of panels (a, c and d) was scaled by a factor of 4 for better visibility.

consequence of aircraft maneuvers were taken into account in the transformation by projecting the laser beam on the local vertical axis with respect to ground. An aircraft speed of $200-250$ m/s results in a horizontal resolution of $12-15$ km for a 1 min integration period. The photon count profiles were then converted to temperature profiles by hydrostatic top-down integration in a similar way as for the ground-based CORAL instrument (B. Kaifler & Kaifler, 2021). In this step, the profiles were smoothed vertically to a resolution of 1,500 m to increase the signal-to-noise ratio and thus allow for a larger vertical extent of the retrieved temperature profiles. In a final step, the vertical coordinate of the temperature profiles retrieved from lidar observations was shifted, taking into account the instantaneous flight altitude. The temperature retrieval also provides estimates of temperature uncertainty which is computed from Monte Carlo simulations of the instrument noise and the uncertainty of the initial value used in the hydrostatic integration. More details on the retrieval and error estimation can be found in B. Kaifler and Kaifler (2021).

The resulting temperature data set $T(t, z)$ as function of time t and altitude z at 1 min × 1,500 m resolution is shown in Figure 4a. Vertical lines mark the start and end times of legs 1 and 2. From the temperature data, perturbations that may be interpreted as signatures of gravity waves are evident. The occurrence and amplitude of these perturbations strongly depend on the geographic location. As the aircraft crosses the mountain range twice at about 00:00 UT and 01:00 UT, the perturbation pattern appears to be mirrored with respect to the time when the aircraft reversed course. Rapp et al. (2021) show in their Figure 12 ALIMA temperature perturbations for ST08 that are in good agreement with ECMWF IFS data prepared in the same way. The IFS data thus provide an independent confirmation of the presence and magnitude of temperature perturbations during ST08.

In order to analyze the spatial properties of gravity waves and relate these to the underlying topography, we transformed the time-resolved temperature profiles to a spatial grid representing distance along the flight track. The distance was calculated on a great circle with the origin located at the end of leg 1 or the start of leg 2,
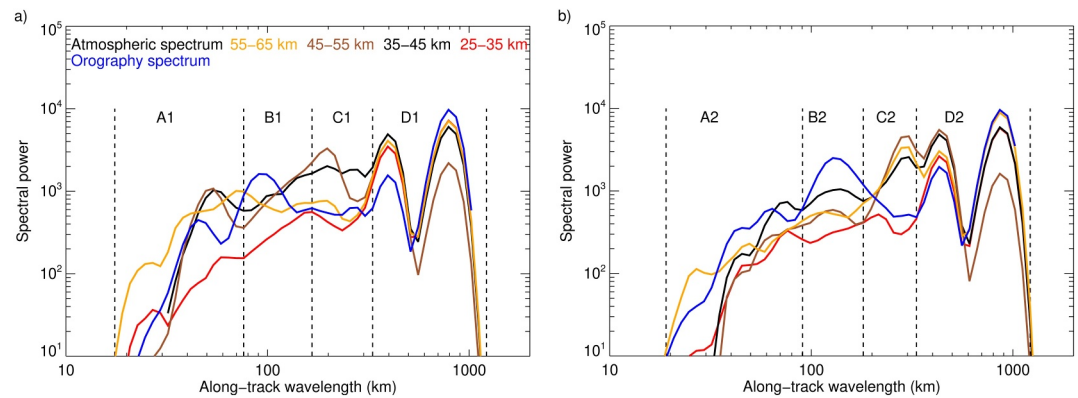
Figure 5. Mean spectral power of $T(r,z)$ in the altitude ranges given in the legend and for the orography for leg 1 (panel a) and leg 2 (panel b). The orography spectrum was normalized such that spectral power integrated between 4 and 1,024 km wavelength equals the integrated power of the atmospheric spectrum at 55–65 km. The dashed lines mark the spectral ranges that were used to separate gravity waves scales. See text for details.

respectively, such that position 0 km in Figures 4c and 4d is located at the turning point above the Pacific (see Figure 2). The horizontal spacing of the temperature profiles is irregular because of the varying ground speed of the aircraft. To simplify the analysis, we interpolated the temperature profiles on a regular distance grid r with 2 km horizontal spacing.

Figures 4c and 4d show the interpolated temperature perturbations $T' = T - T_0$ with the background removed in order to highlight gravity wave-induced perturbations. The background temperature profile T_0 was determined upstream at the turning point of the aircraft (00:26 UT) and smoothed with a 5 km running mean in the vertical. Maximum perturbations exceed 30 K and are much larger than the uncertainty of the temperature measurement that increases with altitude for each of the three detection channels and is below 2 K for most of the 20–55 km altitude range (Figure 4b).

2.3.1. Separation of Wave Packets and Estimation of Wave Parameters

As evident from Figures 4c and 4d, ALIMA temperature perturbations are large in amplitude in the stratopause region above and in the lee of the main mountain ridge, but smaller perturbations are also visible throughout the stratosphere and lower mesosphere. Although the pattern is generally similar between the two flight legs, there are also some differences. For example, the striking stripe pattern with nearly vertical phase lines and a periodicity of about 50 km above the main mountain peaks between 40 and 50 km altitude is more pronounced in panel c (leg 1) than in panel d (leg 2).

Because the Andes constitute a quasi two-dimensional barrier with individual peaks embedded in north-south direction, we assume the waves sampled by ALIMA were generated by a superposition of modes that can be characterized by the orography beneath HALO's flight path. To gain insight into the characteristics of those different gravity waves and assess the contributions of orographic modes, we separated wave packets based on their along-track wavelength. This was done by applying one-dimensional wavelet analysis to the temperatures on the spatial grid subsequently for each altitude z using sixth-order Morlet wavelets. The wavelet spectra were stripped of components with non-significant power and averaged over altitude ranges corresponding to the mid stratosphere (25–35 km, red line in Figure 5), the upper stratosphere (35–45 km, black line), the stratopause region (45–55 km, brown line) and the lower mesosphere (55–65 km, yellow line). In addition, we show the spectrum of the orography underneath the flight tracks (blue line). Significant spectral power (values $\sim 10^3$) is found for all scales, and multiple peaks occur, for example, around along-track wavelengths of 55 and 400 km. Peaks at similar wavelengths as in the atmospheric spectra also occur in the orography spectrum, a strong hint that the waves are actually mountain waves generated by flow over orography. We do not expect a perfect agreement since as indicated by Figure 13 in Rapp et al. (2021), mountain waves that were excited by the low-level flow across mountain peaks to the north of the flight track were refracted southeast into the polar night jet and crossed ALIMA's field of view. ALIMA thus observed a superposition of different waves originating from sources located directly below as well as aside the flight track. Since the orography spectrum is based exclusively on the

orography directly below the aircraft and does not include neighboring mountain peaks, we expect some differences between the atmospheric spectra and the orography spectrum.

We divided the spectral range which includes along-track wavelengths ranging from 18 to 1,154 km into four parts with the goal to capture and separate the major spectral peaks visible in Figure 5. We chose the ranges A1 = 18−72 km, B1 = 72−157 km, C1 = 157−314 km and D1 = 314−1154 km for leg 1, and A2 = 20−86 km, B2 = 86−171 km, C2 = 171−314 km and D2 = 314−1154 km for the longer leg 2.

Our next step is to extract temperature perturbations T' within each of the ranges A-D by wavelet analysis. In order to remove contributions from scales other than the selected scale, we set all wavelet coefficients outside the relevant spectral range to zero before computing the inverse transformation. The result is shown in Figure 6. The figure includes eight panels for the two legs and the four spectral ranges, with horizontal scales increasing from top to bottom. We defined regions of interest as rectangular boxes (marked in purple) in the height-distance cross sections. We chose the size and location of these boxes such that they encompass evident wave activity, that is, regions where the temperature amplitude is sufficiently large to discern more or less continuous phase lines associated with assumed gravity wave packets. Within the regions of interest, we then applied a ridge-finding algorithm to T' to track four to 10 phase lines of warm and cold phases. The identified phase lines are shown as black lines in Figure 6. We define the along-track wavelength λ_r of a wave packet as twice the mean horizontal distance between adjacent phase lines. In a last step, we obtained the mean vertical wavelength λ_z from the slope of linear functions $f_j = a_j(z) + b_j$ fitted to j phase lines via

$$\lambda_z(z) = \frac{\lambda_r(z)}{\overline{a_j}}, \tag{1}$$

where the bar denotes the average over j. The results of fits f_j are depicted by green lines in Figure 6.

As evident from Figure 5, the spectral ranges D1 and D2 comprise two peaks. We tried isolating the two peaks by using narrower passbands in the wavelet analysis. However, this attempt was not successful given that we are not dealing with monochromatic waves and narrower passbands diminish reconstructed amplitudes.

2.3.2. Converting Along-Track Wavelengths to Horizontal Wavelengths

The horizontal wavelength λ_h of gravity waves is related to the along-track wavelength λ_r derived from ALIMA measurements by

$$\lambda_h = \lambda_r \sin \beta, \tag{2}$$

with

$$\beta = \Phi - \alpha \tag{3}$$

being the angle between the orientation of the flight track Φ and the orientation of the gravity wave phase lines α in the horizontal plane. Only when $\beta = 90°$, that is, the flight track is perpendicular to the waves' phase lines, the two wavelengths are identical. How do we determine β in order to obtain λ_h, which we will later need to estimate the gravity wave momentum flux? The ALIMA data are purely along-track measurements and provide no information in the cross-track direction. While in principle the wave orientation can be derived from measurements along two approximately parallel flight tracks separated by a few tens of kilometers when assuming a stationary wave field (e.g., Geldenhuys et al., 2023), the spatial separation between the two cross-mountain legs of ST08 is too small. Hence, to obtain an estimate of the wave orientation, in the following we combine our measurement data with results from a Fourier ray model.

The Fourier ray model we employed was previously used to study the propagation of orographic waves excited by small islands (Eckermann et al., 2016). In comparison to the work by Eckermann et al. (2016), the orography of the Andes is much more complex and includes a multitude of peaks distributed over a large area of the south American continent. For the orography we used ASTER data (Figure 2) loaded into a 4096 × 4096 km² model domain with 4 km horizontal resolution. In the Fourier ray model, each component of the Fourier transform of the
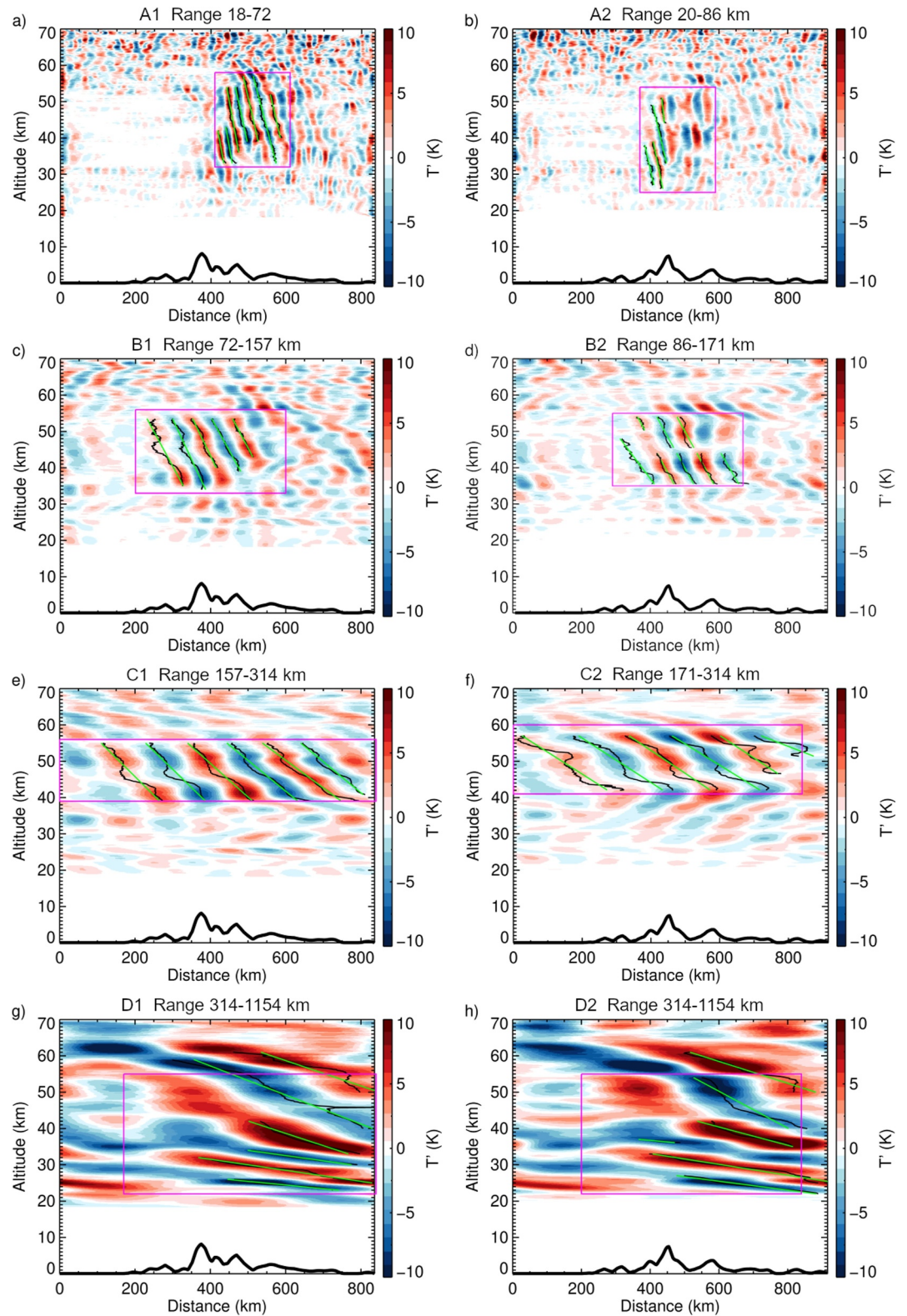
Figure 6. Temperature perturbations for leg 1 (left column) and leg 2 (right column) reconstructed from one-dimensional wavelet analysis of ALIMA data for spectral ranges A to D (from top to bottom). The purple boxes mark the selected regions of interest. The black thin curves indicate the phase lines as determined by the phase tracking algorithm, and the green lines represent linear fits to these curves. The thick black lines show the orography scaled by a factor of 10 for better visibility.

topography is propagated to the next altitude level according to the linear and hydrostatic wave equations including rotation (Broutman et al., 2004). To define the atmospheric background state the waves would be propagating in, we used the profiles of temperature, zonal and meridional wind, and buoyancy frequency shown in Figure 1. The vertical level spacing of the model and the resolution of the background profiles are 500 m from 0 to 80 km altitude. The model evaluates turning points and critical levels for each step, and affected Fourier components are subsequently filtered out. The output of the model is steady-state temperature perturbations $T'_\text{M}(x, y, z)$ at 4 km × 4 km × 0.5 km resolution. Examples of vertical cross-sections of filtered temperature perturbations interpolated along flight tracks are shown in Figure A1.

We used $T'_\text{M}(x, y, z)$ fields to determine the orientation of simulated waves within a horizontal plane. This was accomplished by the application of two-dimensional wavelet analysis to $T'_\text{M}(x, y)$ at a given altitude z using Morlet wavelets with a wavelet scale of λ_h and angle α, the latter rotates the wave within the horizontal plane. We then computed all inverse transforms $\tilde{T}'_\text{M}(x, y, \lambda_h, \alpha)$, revealing the spatial extent and amplitude of any potential gravity wave packet defined by parameters λ_h and angle α. Using the regions of interest as defined in Figure 6 projected onto horizontal planes within the model domain, we computed the average $\widetilde{T'}^2_\text{M}$ along the line resulting from the projection for any given (λ_h, α). By arranging the averages of $\widetilde{T'}^2_\text{M}$ as function of λ_h and α, we created two dimensional spectrograms. Using Equations 2 and 3, a relation between λ_h and α can be determined for each observed wavelength λ_r. This relation is represented by a curve in the spectrograms. An example of such a curve is shown in Figure A2. For each of the λ_r found in ALIMA data we then determined the λ_h and α corresponding to the observed λ_r from the point in the spectrogram where the respective curve describing all potential combinations of λ_h and α intersects a peak in spectral power. Note that any peak in spectral power occurring somewhere along the curve represents a simulated wave packet defined by a combination of λ_h and α that maps to the observed wavelength λ_r. Because we had determined λ_r from ALIMA data, the above described procedure ensures that we only consider those simulated wave packets that had actually been observed by the lidar. For each observed λ_r the procedure was repeated for all altitude levels in steps of 2 km.

We note that relying on the Fourier ray model for determining the wave orientation comes with some significant limitations: (a) the model is a purely linear model and thus cannot simulate wave breaking, (b) solving the hydrostatic equations may lead to biases in wavelength estimates for non-hydrostatic waves, and (c) the model does not take into account wave refraction which may be significant above the Andes. See Section 4.4 for a detailed discussion.

2.3.3. Derivation of Gravity Wave Momentum Flux and Drag

Our goal is to determine the vertical flux of horizontal gravity wave momentum for the regions of interest as defined in Figure 6 following Ern et al. (2004, 2018):

$$F_\text{ph} = 2AB\rho \frac{\lambda_z}{\lambda_h} E_\text{p}, \tag{4}$$

with the prefactors A and B determined according to the supplement of Ern, Hoffmann, and Preusse (2017), the air density ρ from NRLMSIS 2.0 (Emmert et al., 2021) for 12 September 2019 00:00 UT and 52°S latitude and 74°W longitude, the horizontal and vertical wavelengths λ_h and λ_z as determined in Sections 2.3.2 and 2.3.1, and the potential energy density E_p as defined in Ern et al. (2018)

$$E_\text{p} = \frac{1}{2}\left(\frac{g}{N}\right)^2 \overline{\left(\frac{T'}{\bar{T}}\right)^2}. \tag{5}$$

Here, the acceleration due to gravity is $g = 9.81\,\text{m}\,\text{s}^{-2}$ and the buoyancy frequency N is calculated from the background temperature profile $\bar{T}$ estimated over the Pacific ($r < 200$ km). The prefactors are given by

$$A = \left(1 - \frac{\hat{\omega}^2}{N^2}\right) \times \left(1 + \frac{C^2}{m^2}\right)^{-1} \times \left(1 + \left(\frac{f}{m\hat{\omega}}\right)^2 C^2\right)^{1/2} \tag{6}$$

and

$$B = \left(\left(1 - \frac{(N^2 - \hat{\omega}^2)CD}{m^2 + C^2}\right)^2 + \left(\frac{(N^2 - \hat{\omega}^2)mD}{m^2 + C^2}\right)^2\right)^{-1}, \tag{7}$$

using $C = \left(\frac{1}{2H} - \frac{g}{c_s^2}\right)$ and $D = \left(\frac{\gamma - 1}{c_s^2}\frac{g}{N^2}\right)$. $c_s = \sqrt{\frac{\gamma RT}{M}}$ is the speed of sound, $H = \frac{RT}{gM}$ is the scale height evaluated for $T = 250$ K, $\gamma = 1.4$ is the adiabatic constant, $R = 8.31446$ J mol^{-1} K^{-1} is the gas constant, $M = 0.0288$ kg mol^{-1} is the molecular mass of air, $f = 2\Omega \sin \phi$ is the Coriolis parameter with $\Omega = 7.27 \times 10^{-5}$ rad s^{-1}, $\phi = 53°$S is the latitude, and

$$\hat{\omega}^2 = \frac{N^2 k^2 + f^2\left(m^2 + \frac{1}{4H^2}\right)}{k^2 + m^2 + \frac{1}{4H^2}} \tag{8}$$

is the intrinsic gravity wave frequency. The product AB is typically close to unity. However, when the vertical wavelength is large (m is small), AB may become as small as ≈ 0.5. AB may also be <1 for waves with short horizontal wavelengths.

Having determined all variables necessary for computing F_{ph} (Equation 4), we can now derive the drag exerted on the flow by gravity waves as the vertical derivative of F_{ph} scaled inversely by density

$$X = -\frac{1}{\rho}\frac{\partial}{\partial z}F_{ph}. \tag{9}$$

In an intermediate step, before taking the derivative, we smoothed F_{ph} using a 5 km running mean to reduce noise.

2.3.4. Estimation of Uncertainties

We estimated the impact of the uncertainty of temperature profiles retrieved from ALIMA measurements on derived quantities using the Monte Carlo method. We start with perturbing $T(z)$ with random numbers with a Gaussian distribution of standard deviation $\Delta T(z)$ and zero mean at 1.5 km altitude intervals reflecting the vertical resolution of the lidar temperature profile. One hundred such profiles were created and subsequently interpolated to the 100 m vertical grid we used in our analysis. The simulated profiles were then analyzed in exactly the same way as the measurements before. Finally, the uncertainties of λ_r, E_p, F_{ph} and X were found from the standard deviations of the analyzed simulated profiles. We estimated the error of λ_z from the standard deviation of $a_j(z)$ and the uncertainty of $\lambda_r(z)$, which was determined from Monte Carlo simulations based on perturbed temperature fields that include the uncertainty of the temperature measurements. The error is approximately 2 km for leg 1 and 6 km for leg 2.

3. Results

The largest perturbations with T' exceeding 10 K occurred above and in the lee of the mountains (Figures 4c and 4d). By decomposition of the gravity wave field as described above, we were able to identify individual wave packets which are to some degree well confined in altitude and horizontal extent. It is interesting to note that wave packets with small λ_r extend over a smaller horizontal range as compared to those with larger λ_r. Moreover, their phase lines are much steeper and appear almost vertical when drawn at the same scale as used for the other wave packets. Hence, we can expect that the small-scale gravity waves visible in Figures 6a and 6b have large λ_z, while the mid-scale gravity waves, for example, Figures 6e and 6f, have smaller λ_z. The pattern associated with the large-scale perturbations shown in panels g and h defies, however, this simple qualitative relationship between horizontal and vertical scales. We see shallow phase lines below 35 km altitude and then again above 55 km, whereas in between the phase lines are noticeably steeper. As will be shown later, the pattern was formed by two wave packets with vastly different true horizontal scales but similar observed horizontal scales.

Table 1
Altitude-Averaged Parameters of Identified Wave Packets

Label	λ_r range (km)	Z (km)	r (km)	λ_r (km)	β (°)	λ_h (km)	λ_z (km)	$\lambda_{z,disp}$ (km)
A1	18–72	32–58	200	53 ± 2	38 ± 2	33 ± 2	25 ± 4	21.5
B1	72–157	33–56	400	114 ± 1	43 ± 2	77 ± 4	23 ± 2	19.6
C1	157–314	39–56	840	221 ± 1	39 ± 3	138 ± 8	20 ± 2	19.1
D1s	314–1,154	22–55	670	504 ± 2	7 ± 2	62 ± 18	14 ± 2	15.3
D1l	314–1,154	22–55	670	504 ± 2	47 ± 2	369 ± 13	14 ± 2	16.6
A2	20–86	25–54	220	50 ± 3	45 ± 4	35 ± 4	24 ± 8	20.5
B2	86–171	35–55	380	121 ± 1	46 ± 2	87 ± 4	19 ± 2	19.3
C2	171–314	41–60	840	292 ± 3	20 ± 11	101 ± 42	17 ± 2	17.1
D2s	314–1,154	22–55	640	544 ± 4	6 ± 2	54 ± 19	15 ± 6	15.6
D2l	314–1,154	22–55	640	544 ± 4	47 ± 4	395 ± 27	15 ± 6	17.2

Note. The columns are defined as follows: label of wave packet, range of the spectral filter used in the determination of wave packets, vertical extent z, along-track extent r, along-track wavelength λ_r, angle $\beta = \Phi - \alpha$ between flight track and wave phase lines, horizontal wavelength $\lambda_h = \lambda_r \sin \beta$, and vertical wavelength estimated from measurements λ_z and from the mountain wave dispersion relation $\lambda_{z,disp}$. See text for details. Note that two solutions for λ_h for wave packets D with smaller (affix "s") and larger λ_h (affix "l") are included here.

Table 1 provides a summary of wave parameters λ_r and λ_z for each of the eight regions of interest defined in Figure 6 together with the relevant ranges. The profiles of λ_r, λ_h and λ_z for each of the gravity wave packets are shown in Figure 7. By design, the values for λ_r (solid line in Figures 7a and 7b) lie within the respective ranges (borders marked by the gray solid lines) which we used to classify the observed scales. The estimated λ_h are shown as dashed lines. Because the gravity wave phases were sampled by ALIMA at angles smaller than 90° according to Fourier ray model results, λ_h are significantly smaller than λ_r. The values of λ_r (solid lines) vary little with altitude and so do the values of λ_h (dashed lines).

Results for the spectral range D (large observed scales) are unique in the way that the curve representing λ_r in the spectrograms created from the Fourier ray model output passes through two major peaks. The interpretation here is that ALIMA actually sampled two wave packets with different λ_h and α, which map to the same λ_r. Therefore, we provide two solutions: The phase lines of wave packet D1l were sampled at a mean angle of 47°, shifting the horizontal wavelength of this wave packet of 369 km to the observed wavelength of 504 km. In contrast, wave packet D1s was sampled at a much shallower angle of only 7°, and in this case λ_r maps to a λ_h of just 62 km. The latter wave packet thus only appears to be large-scale in our observations because of the orientation of the wave packet relative to the flight path of the airplane, and is in fact small-scale. Similar results were obtained for wave packets D2l and D2s encountered in flight leg 2.

The λ_z of the identified gravity waves are in the order of 20 km with few exceptions (Figures 7c and 7d). Shorter wavelengths down to 8 km were found for wave packets D1 and D2 (red lines) below 32 km altitude. For reference, as last column in Table 1 we added the vertical wavelength obtained from the dispersion relation for mountain waves

$$m^2 = \frac{N^2}{\bar{u}^2} - k^2 \tag{10}$$

which relates the vertical wave number m to the Brunt-Väisälä frequency N, the effective wind speed parallel to the wave vector $\bar{u}$, and the horizontal wavenumber k. Here we have used $\lambda_{z,disp} = 2\pi m^{-1}$ and $k = 2\pi\lambda_h^{-1}$. For N and $\bar{u}$ we used the ECMWF IFS data shown in Figure 1 with $\bar{u} = \sqrt{(u(z)\cos\alpha)^2 + (v(z)\sin\alpha)^2}$ being the horizontal wind projected on the wave vector. We note that our measured λ_z are compatible with derived $\lambda_{z,disp}$ for all wave packets except B1 and D1l, with both packets having deviations of less than 10 % from predicted values.
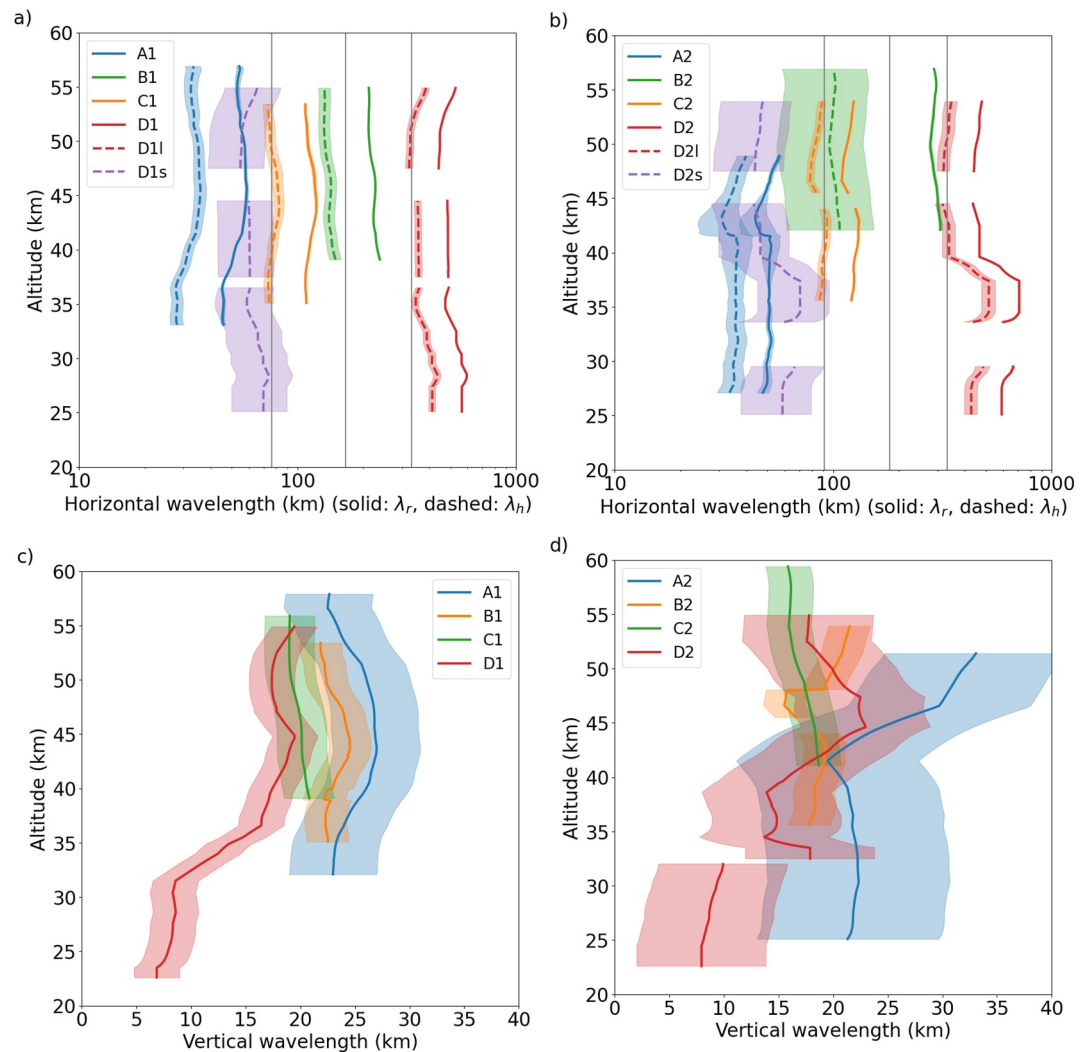
Figure 7. Vertical profiles of horizontal along-track wavelength λ_r (panels a and b, solid lines), horizontal wavelength λ_h (panels a and b, dashed lines) and vertical wavelength λ_z (panels c and d) retrieved from ALIMA data for legs 1 (left) and 2 (right). Each profile is derived from one of the gravity wave packets shown in Figure 6. All profiles were smoothed using a running mean with length 5 km. The shaded regions represent standard errors.

Figure 8 shows vertical profiles of E_p, F_{ph}, and X for each of the wave packets. The largest values of E_p are found for wave packets D (red lines) in both the stratosphere and mesosphere for both flight legs, followed by wave packet A (blue line) for leg 1 and wave packet B (yellow line) again for both legs (Figures 8a and 8b). Values for E_p range between 3 and 60 J kg^{-1}. It is remarkable that a local minimum exists at around 45 km altitude for all wave scales. This altitude coincides with a maximum in horizontal wind speed (Figure 1). Going back to Figure 6, we see an apparent phase shift that results in small T' at this altitude level and thus low E_p. Accordingly, F_{ph} has a local maximum shortly below 40 km altitude (Figures 8c and 8d), resulting in negative drag exerted on the background flow of up to 800 m/s/day at this level (Figures 8e and 8f). Figures 8c and 8d also reveal that the largest part of the momentum flux is carried by small-scale waves with $\lambda_\mathrm{h} < 100$ km (wave packets A, D1s, and D2s; see also Figure 7).

4. Discussion

We first look at the distribution of energy and momentum between waves of different scales and discuss implications. We then discuss evidence leading up to the conclusion that the observed wave event was rather typical and thus representative for the mean atmospheric state in September. We also estimate the contribution of mountain
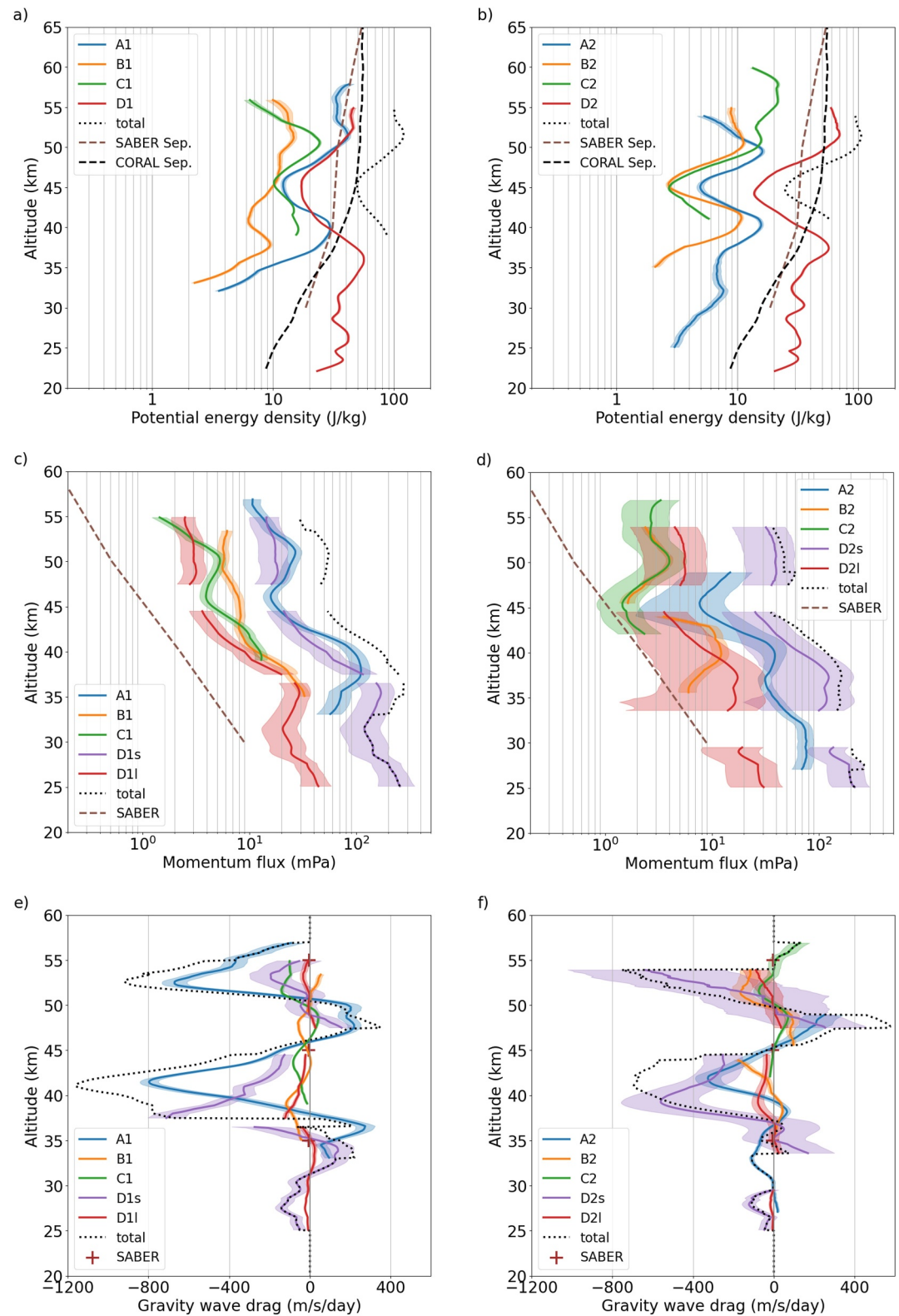
Figure 8. Vertical profiles of E_p (panels a and b), F_{ph} (panels c and d), and X (panels e and f) for legs 1 (left) and 2 (right) smoothed with a 5 km running mean. The colors indicate the wave packets as in Figure 7. The dashed black E_p profile shows the September mean derived from the CORAL lidar data acquired at Río Grande (Reichert et al., 2021). The dashed brown E_p and F_{ph} profiles are for September and 50°S, 70°W from SABER soundings in 2002–2014 (Ern, Trinh, et al., 2017).

waves generated by the Andes mountains to the zonal mean zonal gravity wave drag and weigh in on the question how important these mountain waves are in the zonal mean picture. Finally, we discuss limitations of our analysis.

4.1. Distribution of Energy and Momentum Between Waves of Different Scales

The comparison of E_p and F_{ph} profiles (Figures 8a–8d) reveals an important aspect: Although the temperature amplitude and thus E_p of wave packet A (blue lines, small λ_r) is smaller than that of wave packets D1l and D2l (red lines, large λ_r), the momentum flux carried by wave packet A is actually larger. Though smaller in magnitude, a similar qualitative relationship becomes evident when comparing E_p and F_{ph} profiles associated with wave packets B and C, and we conclude that small-scale waves with weak temperature amplitudes may make a significant contribution to the total momentum flux. This poses at least two challenges for observations: (1) Can low-amplitude, small-scale wave packets still be identified and extracted when they are hidden behind larger-amplitude, larger-scale wave perturbations? This is both a question of signal-to-noise ratio of the measurement and the spectral filtering techniques used. The latter are often designed to extract structures that dominate the amplitude spectrum, but focusing on modes with the largest amplitudes may lead to an underestimation of momentum flux. (2) How far does the momentum flux spectrum extend toward small λ_h, and can waves be resolved down to the smallest relevant scale? If this is not the case, the total momentum flux may again be underestimated.

We solved (1) by using a powerful lidar with a high signal-to-noise ratio and looking at the entire perturbation spectrum. Identifying waves with small but significant spectral power in spectral space allowed us to reconstruct these waves independently and study their individual contributions to the total momentum flux. Judging from E_p profiles (Figures 8a and 8b), we achieved a dynamic range exceeding one order of magnitude. This is sufficient for estimating momentum fluxes associated with waves over a large range of wavelength ratios $\lambda_z \lambda_h^{-1}$ including non-hydrostatic waves, which may have small amplitudes but large $\lambda_z \lambda_h^{-1}$.

Question (2) is less straightforward to answer. The along-track resolution of ALIMA is 12–15 km depending on aircraft speed. As evident from Table 1, ALIMA sampled phase lines of waves at angles <90°, resulting in λ_r being shifted to values larger than λ_h. The actual resolution in λ_h is thus higher than the along-track resolution. For example, for a 40° angle of intersection a resolution of 8–10 km in λ_h is achieved. Since the angle of intersection for most of the wave packets was around 40° or smaller, we conclude that ALIMA was able to observe waves with horizontal scales down to about 32 km (four independent samples per wavelength). Indeed, the smallest λ_h we identified is 33 km (wave packet A1, see Table 1). We argue that there were no gravity waves with relevant amplitudes below this scale present during ST08 for two reasons. First, from the evaluation of the cut-off wavelength we see that waves with $\lambda_h \leq 25$ km encountered a turning level below 40 km altitude and were thus unable to propagate to higher altitudes (Figure 1f). Second, the power in the orographic spectrum (Figure 5) falls off sharply toward smaller wavelengths between 40 and 30 km wavelength along track. The comparison of orographic and atmospheric spectra demonstrates that the atmospheric response follows roughly the orography. This suggests that for waves with wavelengths smaller than ∼30 km along track we should expect a similar drop in amplitude and thus insignificant wave amplitudes. In summary, we conclude that ALIMA was able to resolve all relevant mountain wave scales encountered during this event. It should be noted, however, that this conclusion is based on the analysis of a singular flight. A number of flights would need to be analyzed in order to get a robust and statistically significant estimate of the lower wavelength limit. Unfortunately, this is not possible given that wave propagation conditions during all subsequent flights were heavily impacted by the stratospheric warming.

By averaging F_{ph} in the altitude range 40–50 km we obtained the momentum flux spectrum shown in Figure 9a. Note that we decided to show the momentum flux rather than momentum flux density (F_{ph} normalized by the respective λ_h interval) in order to reflect the fact that we observed discrete wave packets. Figure 9 reveals that most of the gravity wave momentum is carried by gravity waves with $\lambda_h < 70$ km. Though the spectrum includes only few data points, there is a general tendency of decreasing F_{ph} with increasing λ_h. From Equation 4 we expect $F_{ph} \propto k = 2\pi\lambda_h^{-1}$. This relation is represented by straight lines with negative slopes in the double logarithmic plot shown in Figure 9a. In order to test whether our measurement data support such a simple model, we compute a linear fit of the form

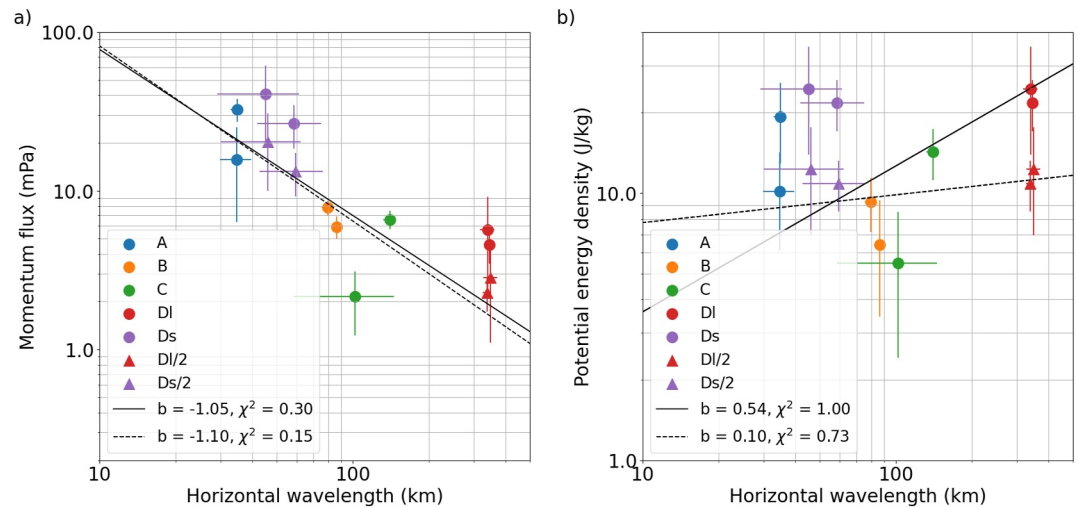$$\log F_{ph}(\lambda_h) = a + b \log \lambda_h \tag{11}$$

Figure 9. (a) Momentum flux spectrum and (b) potential energy density spectrum derived from ALIMA measurements in the 40–50 km altitude range. The data points represented by red and purple circles are upper estimates, while the triangles represent an equal distribution of E_p (see text for details). The triangles are plotted with a small horizontal offset to increase the readability of the error bars.

with fit parameters a and b. Uncertainties of F_{ph} and λ_h are included in the optimization. Using the data points represented by filled circles we obtain $b = -1.05$ (black solid line in Figure 9a). The filled circles representing Ds and Dl were computed as if all the E_p of the two superimposed wave packets would be concentrated in one of the two wave packets. These values therefore represent upper estimates of F_{ph}. Assuming E_p is equally distributed between the two wave packets, we obtain the values marked by triangles and labeled with Ds/2 and Dl/2. In this case the slope increases to $b = -1.10$ (dashed line). The χ^2-values of the fits are 0.30 and 0.15, that is, well below 1, and we conclude that the errors associated with the data points are too large to properly constrain the model (Equation 11). However, both derived slopes (values -1.10 and -1.05) are actually very close to the exponent -1 that is implied by Equation 4. We don't know how E_p is distributed between the two superimposed wave packets for real, but given that the slopes derived for the two discussed cases are similar, we have confidence in our results. Since $k = 2\pi\lambda_h^{-1}$, we find that the spectral dependence is approximately k^1.

If $F_{ph} \propto \lambda_h^{-1}$ as our results suggest, then it follows that other factors in Equation 4 such as λ_z and E_p must be independent of λ_h. Indeed, there is little variation in λ_z between wave packets, with values ranging from 18 to 26 km within the altitude range 40–50 km (Figure 7), and the energy spectrum (Figure 9b) does not show any clear tendency. Including the upper bound estimates for the two superposed wave packets, we obtained a slope of 0.54 (solid line) using the same linear model as for the momentum flux (Equation 4). The slope reduces to 0.10 (dashed line) when we assume equal distribution of E_p between the two wave packets (triangles).

Whether the approximately flat E_p spectrum and a k^1 slope in the momentum flux spectrum are properties unique to primary mountain waves above the Southern Andes or can be assumed valid properties in a more general sense, we can only speculate. We were able to observe deeply penetrating mountain waves only during flight ST08. For later flights, the progressing Sudden Stratospheric Warming prevented their propagation to the upper stratosphere and mesosphere. Using a different analysis technique which does not distinguish between primary mountain waves and other perturbations, we found slopes close to $k^{-5/3}$ for the amplitude spectrum (Knobloch et al., 2023). This result is in stark contrast to the nearly flat mountain wave E_p spectrum derived in this work. From the significantly different slopes we conclude that the mesoscale spectrum in the middle atmosphere cannot be explained by primary mountain waves. Other processes such as secondary wave generation as well as waves from other sources are likely responsible for the steeper spectral slope found by Knobloch et al. (2023).

4.2. Classification of the Observed Wave Event

The question whether the mountain wave event observed during the ≈ 2 hr flight segment of ST08 was representative for the mean state in month September is of importance when we want to assess the contribution of Andes mountain waves to the zonal mean gravity wave drag. If the observations represent a rare, extreme case of mountain waves, we can not evaluate this contribution without knowing how often such events occur. However, there are several indications that the observed waves were moderate and can thus be assumed to be representative for the mean state. BAHAMAS measured positive vertical wave energy fluxes of $EF_z = 1.8\,\mathrm{Wm}^{-2}$ and $2.0\,\mathrm{Wm}^{-2}$ along the two cross mountain legs at 10.4 and 12 km altitude, respectively (see Dörnbrack et al. (2022) for a description of the analysis). Thus, the wave energy fluxes at flight level above the Andes were moderate and smaller than those during later research flights ST10 and ST12 (see Figure 10 in Rapp et al., 2021). The ST08 energy fluxes are also smaller than observed above New Zealand during the Deep Propagating Gravity Wave Experiment (DEEPWAVE) (R. B. Smith et al., 2016). Other evidence can be inferred from comparisons to climatological data sets, for example, from SABER data. Given the greater sensitivity of the SABER instrument to larger-scale perturbations, we compare SABER results to our large-scale wave packets (wave packet D, red line in Figure 8). A multi-year monthly mean E_p profile for the Southern Andes region (Ern, Trinh, et al., 2017) and month September (years 2002–2014; brown dashed lines in Figures 8a and 8b) shows slightly smaller values than E_p derived from ALIMA measurements. On first sight, this suggests that the ST08 mountain wave event was above-average in amplitude. However, given the tendency of the SABER instrument to underestimate temperature perturbations due to wider averaging kernels, without further examination the significance of the comparison is less clear.

Further evidence can be drawn from measurements obtained by the ground-based CORAL lidar located at Río Grande (see map in Figure 2). The mean E_p profile for month September (years 2018–2020) (Reichert et al., 2021, their Figure 7), is comparable in magnitude to the SABER E_p profile and values are slightly lower than our ALIMA results (Figures 8a and 8b). CORAL measures temperature profiles with similar vertical resolution as ALIMA and thus should be capable of producing comparable results in terms of instrument sensitivity. The caveat here is, however, its downstream location to the south-east of the mountain peaks. As evident from Figure 6, the strongest perturbations associated with small to medium-scale waves are confined to regions directly above the mountains. Hence, we expect smaller wave amplitudes at the location of CORAL and thus lower E_p. There are no simultaneous observations by CORAL and ALIMA because CORAL was not in operation during the SOUTHTRAC-GW campaign due to a laser failure.

The fact that ALIMA E_p is roughly comparable to the CORAL September mean E_p suggest an about average or below-average wave activity during ST08. For comparison, N. Kaifler et al. (2020) report for a large mountain wave event CORAL peak E_p values that are a factor of 4–5 larger than the weekly mean, reaching up to 700 J kg^{-1} at 50 km (their Figure 2). The peak E_p associated with large-amplitude mountain waves is thus more than one order of magnitude larger than what we observed with ALIMA. This finding and the comparable means discussed above lead us to the conclusion that the wave event observed during ST08 should be classified as weak to moderate.

4.3. Comparison With Other High-Resolution Airborne Lidar Observations

The only other high-resolution data set acquired by airborne lidar are sodium lidar measurements that were conducted during the DEEPWAVE campaign above the Southern Alps in New Zealand (Fritts et al., 2016). With their north-easterly orientation, the Southern Alps represent a barrier to the westerlies in austral winter in a similar way as the Southern Andes in South America, and are thus a powerful source of mountain waves. Bossert et al. (2018) analyzed lidar measurements in the vicinity of the mountain wave hot spot over the south island. They show momentum flux spectra for altitudes 80–89 km for four passes over Mount Cook, all acquired during the same research flight. The spectra exhibit strong peaks at $\lambda_h \approx 80$, 120, and 220 km near the bottom of their altitude range. In some passes, there are additional weaker peaks at $\lambda_h \approx 50$ and 60 km, but the peak at $\lambda_h \approx 80$ km is by far the strongest. The Bossert et al. (2018) results are thus close to our results which show the largest responses at $\lambda_h = 62$ km (wave packet D1s) and 33 km (wave packet A1). The agreement may be even better given that the horizontal wavelengths derived in Bossert et al. (2018) are likely biased toward larger values, given

their assumption that the flight track crossed wave phase lines at right angles, that is, $\lambda_h = \lambda_r$. We showed in Section 2.3.2 that λ_h can be significantly smaller than λ_r. The comparison of spectral slopes is less conclusive.

Though observed λ_h are similar to our results, any conclusions drawn from the comparison should be taken with a grain of salt given the two different locations, different background profiles, and different boundary conditions. On the other hand, the fact that there are similarities in the observations may be seen as evidence of intrinsic characteristics of mountain waves in the middle atmosphere which do not strongly depend on particular source characteristics or boundary conditions.

4.4. Limitations of Our Analysis

When the ALIMA instrument was designed and the original measurement strategy developed, it was assumed that we would be flying largely parallel to wave vectors of mountain waves, allowing us to determine λ_h, λ_z, T' and finally F_{ph} with high precision. The reality turned out to be different, however. Triggered by the Southern Stratospheric Warming and the shift in the polar vortex, propagation conditions for mountain waves above the Southern Andes changed dramatically from the climatological mean. ALIMA observed a rather complex pattern of superimposed waves with wave vectors pointing in different directions, and determining the waves' orientation in the horizontal plane became a major problem. The Fourier ray model we employed is a linear model. Hence, we cannot expect realistic wave amplitudes for non-linear cases such as wave breaking, which ALIMA has observed. However, since we relied on model wave amplitudes only for locating wave packets in the λ_h-α spectral space and used measured T' in momentum flux calculations, we believe our approach is sound. A bigger limitation comes from the fact that the model is steady-state and does not simulate transient forcing, as was clearly the case hours before and during flight ST08 (Alexander et al., 2023). But we can employ the same argument also in this case: using measured T' and λ_r (subsequently transformed to λ_h) in momentum flux calculations rather than model results yields robust estimates for F_{ph}. The only use of the model data was to transform λ_r, which come from observations, to λ_h, and retrieved F_{ph} profiles should be correct as long as the model produces the correction orientation of the waves. We want to point out that the model has one significant limitation in this regard: the horizontal wind field is assumed homogeneous across the model domain, that is, the model is not capable of producing wave refraction. Using data from operational numerical weather prediction models such as ECMWF IFS instead of the Fourier ray model for determination of wave orientations solves this particular problem but results in another problem: the small-scale waves carrying the largest momentum flux are not represented in operational ECMWF IFS data, likely due to insufficient model resolution. What we would need is high-resolution (~ 2 km) mesoscale modeling. Because no high-resolution 3D numerical simulations with realistic wind fields were available for this study, we accept the uncertainty in wave orientation resulting from the use of the linear Fourier ray model and discuss the implications below.

How reliable are our results given that we don't know the true orientation of the waves? Let us first consider the potential worst case which is wave packet D1s with a shallow angle of intersection of only 7°. Assuming an uncertainty in the waves' orientation of 5° puts the derived λ_h in the interval 18–105 km. The low end is clearly unrealistic given that waves with $\lambda_h < 24$ km encountered a turning level at about 35–40 km altitude (see Section 2.1). Taking 24 km as the lowest possible value increases F_{ph} by a factor of 2.6 relative to our estimate ($\lambda_h = 62$ km), while the value 105 km decreases F_{ph} by a factor of 1.7. For larger angles of intersection the impact is much less severe. In case of wave packet A1 ($\beta = 38°$), for example, the λ_h-range for the same 5° uncertainty is 24–36 km and the derived F_{ph} change by factors of approximately 1.4 and 1.1, respectively. From the two examples discussed here it is clear that there is no single answer. It all depends on what we assume as "truth." The spectrograms determined from the Fourier ray model output (examples are shown in Appendix A) suggest that for the meteorological situation during the flight ST08, neglecting refraction may result in worst case errors in the orientation of waves of 5° to 15° near the top of our altitude range. Generally, we believe the error is much smaller at lower altitudes because the rotation of the wave vector increases with altitude. It is also important to note that, as discussed in Appendix A, refraction caused the waves to rotate clockwise (smaller α), resulting in larger λ_h (Equation 2) and thus lower estimated F_{ph}. This finding is compatible with the above discussed fact that a shift to smaller wavelengths would result in unrealistic small λ_h in some cases, making an anti-clockwise rotation less likely. Although we were able to estimate the effect of wave refraction from our measurements and the Fourier ray model output for some altitudes (see Appendix A), we do not trust these estimates enough to warrant a correction

of α. In summary, we think neglecting refraction results in an overestimation of F_{ph} of up to 70% for waves sampled at shallow angles and up to 20% for waves with $\beta > 40°$.

That the combination of vertical information provided by lidar and horizontal information from other sources, in our case the orientation of the sampled waves estimated from the Fourier ray model output, can increase uncertainty was already noted by Gupta, Reichert, et al. (2024). Since there is no technology available so far which allows profiling with sufficiently high resolution in two dimensions, merging of measurement data and modeling results will be required in the foreseeable future. To reduce uncertainties, better strategies should be developed. A promising path forward is sub-kilometer-scale resolution numerical modeling and validation of these models using measurements. One step in this direction is the work by Kruse et al. (2022) who validated gravity waves simulated with high-resolution models (the highest resolution was 3 km) above the Andes and the Drake Passage against Atmospheric Infrared Sounder (AIRS) observations.

Finally, it must be noted that the results presented in this work assume that different spectral gravity wave modes are independent and their contributions to E_P and F_{ph} are due to linear superposition. However, the vertically propagating mountain waves likely change their intrinsic frequencies with height due to the vertically varying wind. When such waves reach their turning levels, they are reflected and lead to an accumulation in the magnitude of F_{ph}. We believe these effects are small, but without high-resolution modeling we cannot provide any quantitative estimates.

5. Summary and Conclusions

The airborne lidar ALIMA provided temperature measurements with both high horizontal ($\sim$10–12 km) and high vertical (1.5 km) resolution from about 20 to 70 km altitude. Using ALIMA data acquired above the Southern Andes, in this work we derived for the first time spectra of the vertical flux of horizontal momentum carried by mountain waves in the upper stratosphere and lower mesosphere. Our main findings are:

1. The Andes mountain ridge generates a spectrum of mountain waves with horizontal wavelengths ranging from $\sim$33–395 km in the middle atmosphere.
2. The superimposing mountain waves can exhibit a complex structure which is difficult to disentangle for along track sampling instruments; small-scale structures can be shifted to large observed horizontal scales depending on the angle of intersection.
3. The mountain wave momentum flux at 40–50 km altitude peaks at around $\lambda_h = 45$ km and the spectral dependence is of the form λ_h^x with $x = -1.0$ to -1.2.
4. More than 80% of the mountain wave momentum flux resolved in ALIMA data at 40–50 km is carried by waves with $\lambda_h < 100$ km.

Based on our findings, we conclude that existing observation-based climatologies underestimate the gravity wave momentum flux in the middle atmosphere because of insufficient measurement resolution. This is in particular true for satellite-based limb sounder instruments such as SABER which typically do not resolve horizontal scales smaller than $\sim$100 km. We note that this work is a singular case study and more observations with ALIMA or similar instruments are needed to characterize the mountain wave spectrum with high significance. If it is possible to derive a kind of "universal" mountain wave spectrum, the shape of the spectrum could be used to estimate and potentially correct biases in momentum flux measurements by instruments which do not resolve the full spectral range. In that sense, high-resolution airborne lidar measurements can make a significant contribution to improving estimates of the global gravity wave momentum budget in the middle atmosphere.

Inclusion in Global Research Statement

Appendix A: Determining the Orientation of Waves From Fourier Ray Model Data

We analyzed the model output T'_M in the same way as the ALIMA data by sampling and interpolating T'_M along the flight track of the aircraft and spectrally filtering the data using the same ranges as described in Section 2. The

resulting model cross sections are shown in Figure A1. The general appearance of the wave pattern is similar to the wave-induced temperature perturbations probed by ALIMA and shown in Figure 6. In particular, the vertical wavelengths appear to be reproduced correctly by the model. One notable difference, however, is the growth of wave amplitudes with altitude. Because the model does not have a saturation scheme which limits the wave amplitudes, perturbations can grow to very large values. This limitation becomes particularly evident for altitudes above 50 km where the perturbations are much larger compared to the ALIMA observations. But since, in the following, we analyze only the horizontal structure of the perturbations and do not evaluate wave amplitudes, incorrect model amplitudes do not affect our results.

In order to determine the azimuth angle α of gravity wave phase lines in a horizontal plane, in a first step we applied 2-dimensional wavelet analysis to the modeled $T'_M(x, y)$ using 6th order Morlet wavelets as described in N. Kaifler et al. (2017). The wavelet analysis decomposes $T'_M(x, y)$ into perturbations characterized by combinations of wavelet scale s and angle of the wavelet α. Choosing $s = 4 \times 2^{j/8}$ with $j = 1, \ldots, 20$ results in horizontal scales λ_h between 19 and 553 km according to $\lambda_h = 2\pi s / (|k_0| \cdot 4)$ with $|k_0| = 5.336$ km^{-1} (see Kirby, 2005). We rotated the wavelets in steps of 5°, where $\alpha = 0°$ corresponds to phase lines oriented in the north-south direction and $\alpha = 45°$ corresponds to phase lines oriented from north-west to south-east. For each combination (s, α) we reconstructed the corresponding $T'_M(x, y)$. Figures A2b and A2d show two examples of reconstructed $T'_M(x, y, z = 40$ km$)$: $\lambda_h = 58$ km, $\alpha = 35°$ and $\lambda_h = 328$ km, $\alpha = 0°$, corresponding to wave packets D1s and D1l at this altitude. We calculated the mean T'^2_M along the flight track (black lines) and, in a second step, arrayed these values such as to form two-dimensional spectrograms $T'^2_M(\lambda_h, \alpha)$. The example shown in Figure A2c for $z = 40$ km reveals multiple local peaks corresponding to gravity waves with different horizontal scales and orientation of their phase lines. The spectrogram for leg 2 is very similar, and when increasing the altitude, the spectral amplitudes may change but the distribution of peaks in terms of λ_h and α remained mostly unchanged (not shown). The largest T'^2_M are found for $\alpha \approx 0°$, that is, phase lines oriented approximately north-south and thus roughly parallel to the mountain ridge. Horizontal and along-track wavelengths are related through the projection of the phase lines onto the flight path: $\lambda_h = \lambda_r \sin \beta$ with $\beta = \Phi - \alpha$, where Φ is the azimuth angle of the flight track (see the sketch in Figure A2a). This function can be solved for $\lambda_r = $ const and α treated as independent and λ_h as dependent variable. In the example shown in Figure A2c, the solution for $\lambda_r = 488$ km is marked as dashed line. The local peak with the largest T'^2_M along this line identifies the dominant gravity wave packet, and the corresponding parameters α and λ_h describing the wave packet can be read from the coordinates of the peak. From the example shown in Figure A2, we concluded that ALIMA sampled the dominant wave packet at a shallow angle which results in a large difference between λ_h and λ_r (wave packet D1s). In addition to the dominant peak, the dashed line passes through two more peaks at $\lambda_h \approx 100$ km and $\lambda_h \approx 320$ km. The T'^2_M associated with these peaks are much weaker, suggesting that E_p of the corresponding wave packets are also significantly smaller. Furthermore, given that $F_{ph} \propto \lambda_h^{-1}$ (see Section 4.1), the relative contribution of the two weaker wave packets to the total F_{ph} is even smaller. We nonetheless added the wave packet associated with $\lambda_h = 328$ km (wave packet D1l) to our list to get an upper estimate on the potential contribution. For the other observed wave packets with smaller λ_r we found only one solution for λ_h in each case.

Figure A3 shows two more examples of spectrograms and curves for the observed wavelengths 52 km (wave packet A2) and 127 km (wave packet B2). We note that these curves meet the modeled spectral peaks just at their edges, which illustrates the limitations of the Fourier ray model. We assume that most inaccuracies result from the inability of the Fourier ray model to produce wave refraction, which can be significant in the Southern Andes region due to the strong wind gradients induced by the polar vortex. Rapp et al. (2021) analyzed ERA5 fields for 00:00 UTC, that is, when the aircraft crossed the mountain range for the first time (their Figure 13). At 10 hPa the phase lines of the mountain waves were oriented approximately perpendicular to the south-westerly to westerly winds ($\alpha > 0°$). At 1 hPa the wind had turned to a northwesterly flow and the phase lines had rotated into the wind, resulting in phase lines that were approximately oriented in north-south direction ($\alpha \approx 0°$).

This clockwise rotation of the wave vector is also evident in our measurement data when combined with Fourier ray modeling. Because the Fourier ray model cannot produce wave refraction, peaks in the spectrograms remain always at the same spot within the spectrogram and only spectral intensities may vary as modes are filtered out with increasing altitude. Figure A3 shows the spectrograms for leg 2 at 50 km altitude for the observed wavelengths 52 and 127 km. The dashed line in Figure A3a meets the edge of the smaller of the two
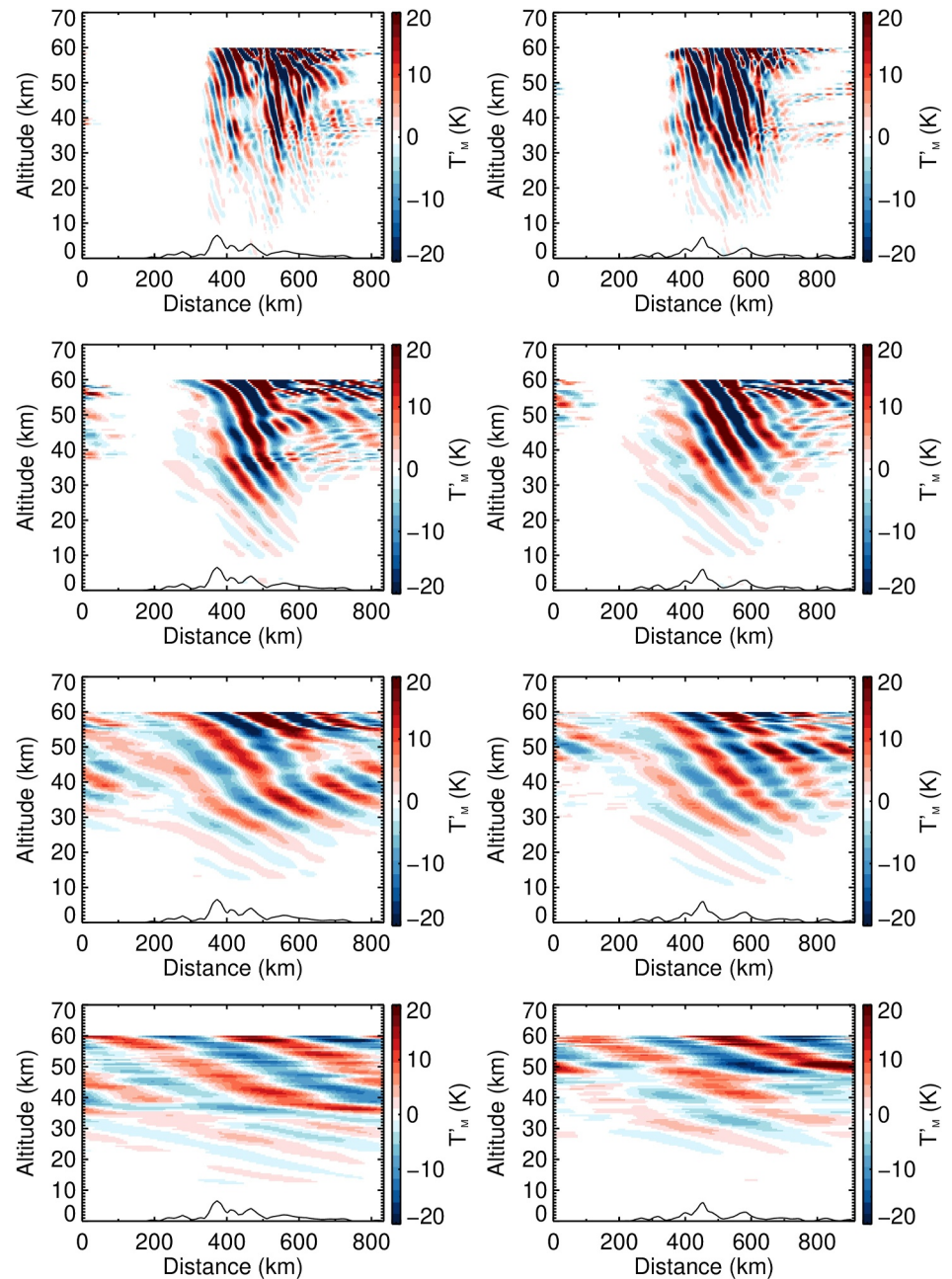
Figure A1. Modeled temperature perturbations for legs 1 (left column) and 2 (right column) and ranges A-D (top to bottom) as in Figure 6.

peaks that is located at $\alpha \approx 10°$ at location $\alpha \approx 0°$. Knowing from Rapp et al. (2021) that the wave vector rotates clockwise due to refraction, that is, α decreases, we add 15° to the α determined from the Fourier ray model to compensate for this effect. The shifted curve shown as a solid line in Figure A3 passes right through the center of the peak, suggesting that a rotation of the Fourier ray model fields by 15° matches our lidar measurement. Assuming this assumption is correct, we can determine the error which the Fourier ray model's inability to produce refraction causes in our analysis. The peak in the model is located at $\alpha \approx 10°$, whereas in reality, according to the rotation, the peak should be at $-5°$. The solution our analysis yields is 0° and the error in this case would be $-5°$.
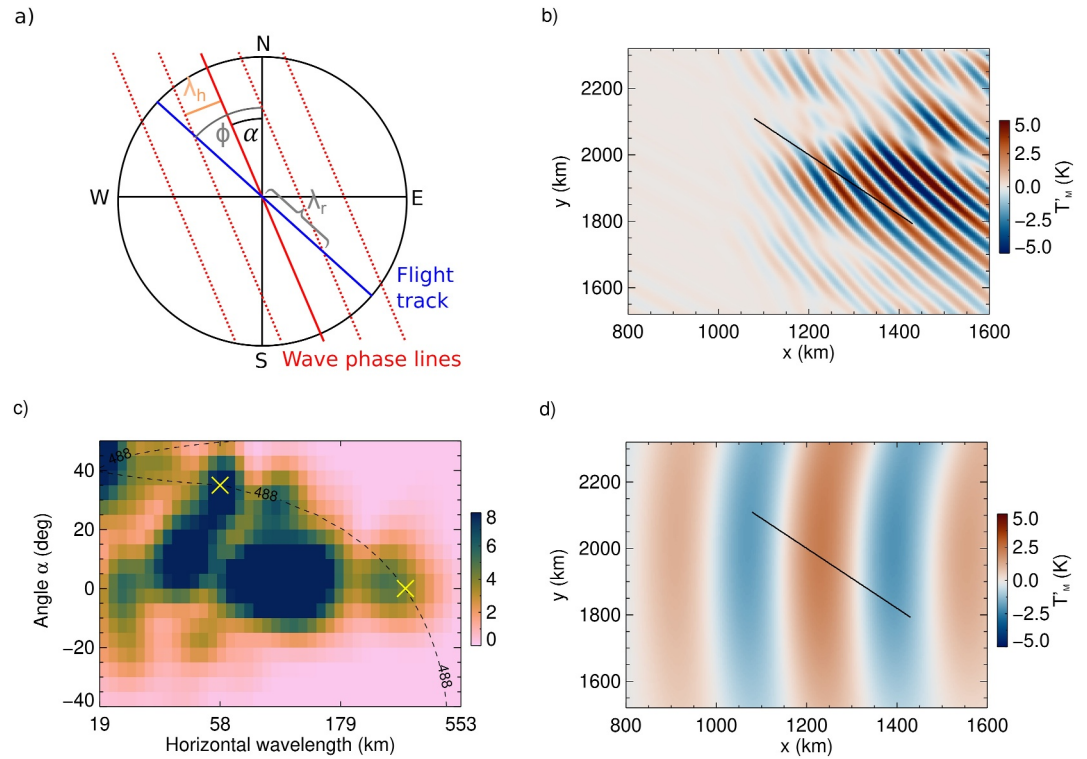
Figure A2. (a) Definition of phase line angle α, flight track orientation Φ, horizontal wavelength λ_h, and observed wavelength λ_r. (b) and (d) Two reconstructions of $T'_M(x,y)$ showing gravity waves with $\lambda_h = 58$ km, $\alpha = 35°$ and $\lambda_h = 328$ km, $\alpha = 0°$. The black lines indicate the flight track. (c) Spectrogram showing $T'^2_M(\lambda_h, \alpha)$ averaged along the flight track. The dashed curve represents all points (λ_h, α) with $\lambda_r = 488$ km. The two reconstructions shown in panels (b and d) are marked by yellow crosses. All plots are for $z = 40$ km.

The situation for the wave with $\lambda_r = 127$ km (Figure A3b) is similar. Again, the curve shifted by 15° (solid line) passes right through the center of the peak. This time, however, the peak is located at $\alpha \approx 0°$, whereas the solution provided by our analysis is also 0°. Following that, we estimate the error to be $-15°$ in this case.

These two examples demonstrate the error that neglecting refraction can introduce in our analysis. Generally, the refraction and thus the error is altitude dependent. At 50 km altitude, the waves have propagated through the strongest wind shears, and the examples shown in Figure A3 may be regarded as the worst case. Indeed, at 40 km altitude (Figure A2) the error seems to be much smaller, as shifting the curve to larger α would result in the curve
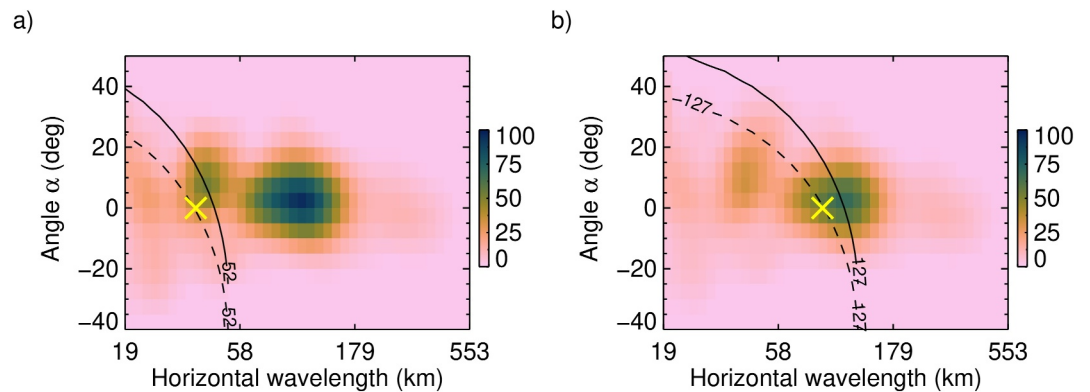

Figure A3. Spectrograms for leg 2 and 50 km altitude: (a) Wave packet A2 and (b) wave packet B2. The dashed curve represents the solutions for $\lambda_r = 52$ km and for $\lambda_r = 127$ km, the solid line the same solutions with α shifted by 15°. The yellow crosses mark the best solution as determined by our analysis algorithm.

missing the peak at $\lambda_h = 58$ km. Note that this elongated peak is actually a superposition of two peaks, and the curve is supposed to select only the upper part (large α). The other peaks in the spectrogram belong to waves with different observed wavelengths.

Data Availability Statement

From the HALO database aircraft location data (BAHAMAS, 2019) and lidar data (ALIMA, 2023) are available. GRACILE data used in this work is attributed to Ern, Trinh, et al. (2017). Atmospheric density profiles were obtained from the NASA CCMC Instant Run System (NRLMSIS, 2023). The facilities of NASA Earthdata were used to download ASTER digital elevation model data (ASTER, 2023).

References

Abrams, M., Crippen, R., & Fujisada, H. (2020). ASTER global digital elevation model (GDEM) and ASTER global water body dataset (ASTWBD). *Remote Sensing*, *12*(7), 1156. https://doi.org/10.3390/rs12071156

Alexander, P., de la Torre, A., Llamedo, P., Hierro, R., Marcos, T., Kaifler, B., et al. (2023). The coexistence of gravity waves from diverse sources during a SOUTHTRAC flight. *Journal of Geophysical Research: Atmospheres*, *128*(5), e2022JD037276. https://doi.org/10.1029/2022JD037276

ALIMA. (2023). St08_20190911a_alima_t1z1500.nc [Dataset]. *HALO Database, German Aerospace Center*. Retrieved from https://halo-db.pa.op.dlr.de/dataset/10176

ASTER. (2023). Aster global digital elevation model netcdf v003 [Dataset]. *NASA Earthdata*. Retrieved from https://search.earthdata.nasa.gov

BAHAMAS. (2019). St08_20190911a_bahamas.nc [Dataset]. Retrieved from https://halo-db.pa.op.dlr.de/dataset/6561.HALOdatabase, GermanAerospaceCenter

Bossert, K., Fritts, D. C., Heale, C. J., Eckermann, S. D., Plane, J. M. C., Snively, J. B., et al. (2018). Momentum flux spectra of a mountain wave event over New Zealand. *Journal of Geophysical Research: Atmospheres*, *123*(18), 9980–9991. https://doi.org/10.1029/2018JD028319

Broutman, D., Rottman, J. W., & Eckermann, S. D. (2004). Ray methods for internal waves in the atmosphere and ocean. *Annual Review of Fluid Mechanics*, *36*(1), 233–253. https://doi.org/10.1146/annurev.fluid.36.050802.122022

de Wit, R. J., Janches, D., Fritts, D. C., Stockwell, R. G., & Coy, L. (2017). Unexpected climatological behavior of MLT gravity wave momentum flux in the lee of the Southern Andes hot spot. *Geophysical Research Letters*, *44*(2), 1182–1191. https://doi.org/10.1002/2016GL072311

Dörnbrack, A., Bechtold, P., & Schumann, U. (2022). High-resolution aircraft observations of turbulence and waves in the free atmosphere and comparison with global model predictions. *Journal of Geophysical Research: Atmospheres*, *127*(16). https://doi.org/10.1029/2022JD036654

Dörnbrack, A., Kaifler, B., Kaifler, N., Rapp, M., Wildmann, N., Garhammer, M., et al. (2020). Unusual appearance of mother-of-pearl clouds above El Calafate, Argentina (50°21′S, 72°16′W). *Weather*, *75*(12), 378–388. https://doi.org/10.1002/wea.3863

Eckermann, S. D., Broutman, D., Ma, J., Doyle, J. D., Pautet, P.-D., Taylor, M. J., et al. (2016). Dynamics of orographic gravity waves observed in the mesosphere over the Auckland Islands during the deep propagating gravity wave experiment (DEEPWAVE). *Journal of the Atmospheric Sciences*, *73*(10), 3855–3876. https://doi.org/10.1175/JAS-D-16-0059.1

Eckermann, S. D., & Preusse, P. (1999). Global measurements of stratospheric mountain waves from space. *Science*, *286*(5444), 1534–1537. https://doi.org/10.1126/science.286.5444.1534

Emmert, J. T., Drob, D. P., Picone, J. M., Siskind, D. E., Jones, M., Jr., Mlynczak, M. G., et al. (2021). NRLMSIS 2.0: A whole-atmosphere empirical model of temperature and neutral species densities. *Earth and Space Science*, *8*(3), e2020EA001321. https://doi.org/10.1029/2020EA001321

Ern, M., Hoffmann, L., & Preusse, P. (2017). Directional gravity wave momentum fluxes in the stratosphere derived from high-resolution AIRS temperature data. *Geophysical Research Letters*, *44*(1), 475–485. https://doi.org/10.1002/2016GL072007

Ern, M., Preusse, P., Alexander, M. J., & Warner, C. D. (2004). Absolute values of gravity wave momentum flux derived from satellite data. *Journal of Geophysical Research*, *109*(D20). https://doi.org/10.1029/2004JD004752

Ern, M., Trinh, Q. T., Preusse, P., Gille, J. C., Mlynczak, M. G., Russell, J. M., III., & Riese, M. (2017). GRACILE: A comprehensive climatology of atmospheric gravity wave parameters based on satellite limb soundings, link to data in NetCDF format [Dataset]. PANGAEA. (Supplement to: Ern, M et al. (2018): GRACILE: a comprehensive climatology of atmospheric gravity wave parameters based on satellite limb soundings. Earth System Science Data, 10(2), 857-892. https://doi.org/10.5194/essd-10-857-2018). https://doi.org/10.1594/PANGAEA.879658

Ern, M., Trinh, Q. T., Preusse, P., Gille, J. C., Mlynczak, M. G., Russell, J. M., III., & Riese, M. (2018). GRACILE: A comprehensive climatology of atmospheric gravity wave parameters based on satellite limb soundings. *Earth System Science Data*, *10*(2), 857–892. https://doi.org/10.5194/essd-10-857-2018

Fritts, D. C. (1984). Gravity wave saturation in the middle atmosphere: A review of theory and observations. *Reviews of Geophysics*, *22*(3), 275–308. https://doi.org/10.1029/RG022i003p00275

Fritts, D. C., Lund, T. S., Wan, K., & Liu, H.-L. (2021). Numerical simulation of mountain waves over the southern Andes. Part II: Momentum fluxes and wave–mean-flow interactions. *Journal of the Atmospheric Sciences*, *78*(10), 3069–3088. https://doi.org/10.1175/JAS-D-20-0207.1

Fritts, D. C., Smith, R. B., Taylor, M. J., Doyle, J. D., Eckermann, S. D., Dörnbrack, A., et al. (2016). The Deep Propagating Gravity Wave Experiment (DEEPWAVE): An airborne and ground-based exploration of gravity wave propagation and effects from their sources throughout the lower and middle atmosphere. *Bulletin of the American Meteorological Society*, *97*(3), 425–453. https://doi.org/10.1175/BAMS-D-14-00269.1

Garcia, R. R., Smith, A. K., Kinnison, D. E., de la Álvaro, C., & Murphy, D. J. (2017). Modification of the gravity wave parameterization in the whole atmosphere community climate model: Motivation and results. *Journal of the Atmospheric Sciences*, *74*(1), 275–291. https://doi.org/10.1175/JAS-D-16-0104.1

Geldenhuys, M., Kaifler, B., Preusse, P., Ungermann, J., Alexander, P., Krasauskas, L., et al. (2023). Observations of gravity wave refraction and its causes and consequences. *Journal of Geophysical Research: Atmospheres*, *128*(3), e2022JD036830. https://doi.org/10.1029/2022JD036830

Gupta, A., Reichert, R., Dörnbrack, A., Garny, H., Eichinger, R., Polichtchouk, I., et al. (2024). Estimates of southern hemisphere gravity wave momentum fluxes across observations, reanalyses, and kilometer-scale numerical weather prediction model. *Journal of the Atmospheric Sciences*, *81*(3), 583–604. https://doi.org/10.1175/JAS-D-23-0095.1

Gupta, A., Sheshadri, A., Alexander, M. J., & Birner, T. (2024). Insights on lateral gravity wave propagation in the extratropical stratosphere from 44 years of ERA5 data. *Geophysical Research Letters*, *51*(14), e2024GL108541. (e2024GL108541 2024GL108541). https://doi.org/10.1029/2024GL108541

Hendricks, E. A., Doyle, J. D., Eckermann, S. D., Jiang, Q., & Reinecke, P. A. (2014). What is the source of the stratospheric gravity wave belt in austral winter? *Journal of the Atmospheric Sciences*, *71*(5), 1583–1592. https://doi.org/10.1175/JAS-D-13-0332.1

Hindley, N. P., Mitchell, N. J., Cobbett, N., Smith, A. K., Fritts, D. C., Janches, D., et al. (2022). Radar observations of winds, waves and tides in the mesosphere and lower thermosphere over South Georgia island (54°S, 36°W) and comparison with WACCM simulations. *Atmospheric Chemistry and Physics*, *22*(14), 9435–9459. https://doi.org/10.5194/acp-22-9435-2022

Hindley, N. P., Wright, C. J., Smith, N. D., & Mitchell, N. J. (2015). The southern stratospheric gravity wave hot spot: Individual waves and their momentum fluxes measured by COSMIC GPS-RO. *Atmospheric Chemistry and Physics*, *15*(14), 7797–7818. https://doi.org/10.5194/acp-15-7797-2015

Hoffmann, L., Grimsdell, A. W., & Alexander, M. J. (2016). Stratospheric gravity waves at southern hemisphere orographic hotspots: 2003–2014 AIRS/Aqua observations. *Atmospheric Chemistry and Physics*, *16*(14), 9381–9397. https://doi.org/10.5194/acp-16-9381-2016

Hoffmann, L., Xue, X., & Alexander, M. J. (2013). A global view of stratospheric gravity wave hotspots located with atmospheric infrared sounder observations. *Journal of Geophysical Research: Atmospheres*, *118*(2), 416–434. https://doi.org/10.1029/2012JD018658

Huang, K. M., Liu, A. Z., Zhang, S. D., Yi, F., Huang, C. M., Gong, Y., et al. (2017). Simultaneous upward and downward propagating inertia-gravity waves in the MLT observed at Andes Lidar Observatory. *Journal of Geophysical Research: Atmospheres*, *122*(5), 2812–2830. https://doi.org/10.1002/2016JD026178

Huang, K. M., Liu, H., Liu, A. Z., Zhang, S. D., Huang, C. M., Gong, Y., & Ning, W. H. (2021). Investigation on spectral characteristics of gravity waves in the MLT using lidar observations at Andes. *Journal of Geophysical Research: Space Physics*, *126*(4), e2020JA028918. https://doi.org/10.1029/2020JA028918

Kaifler, B., & Kaifler, N. (2021). A Compact Rayleigh Autonomous Lidar (CORAL) for the middle atmosphere. *Atmospheric Measurement Techniques*, *14*(2), 1715–1732. https://doi.org/10.5194/amt-14-1715-2021

Kaifler, N., Kaifler, B., Dörnbrack, A., Rapp, M., Hormaechea, J. L., & de la Torre, A. (2020). Lidar observations of large-amplitude mountain waves in the stratosphere above Tierra del Fuego, Argentina. *Scientific Reports*, *10*(1), 1–10. https://doi.org/10.1038/s41598-020-71443-7

Kaifler, N., Kaifler, B., Ehard, B., Gisinger, S., Dörnbrack, A., Rapp, M., et al. (2017). Observational indications of downward-propagating gravity waves in middle atmosphere lidar data. *Journal of Atmospheric and Solar-Terrestrial Physics*, *162*, 16–27. (Layered Phenomena in the Mesopause Region). https://doi.org/10.1016/j.jastp.2017.03.003

Kirby, J. (2005). Which wavelet best reproduces the Fourier power spectrum? *Computers I& Geosciences*, *31*(7), 846–864. https://doi.org/10.1016/j.cageo.2005.01.014

Knobloch, S., Kaifler, B., Dörnbrack, A., & Rapp, M. (2023). Horizontal wavenumber spectra across the middle atmosphere from airborne lidar observations during the 2019 southern hemispheric SSW. *Geophysical Research Letters*, *50*(14), e2023GL104357. https://doi.org/10.1029/2023GL104357

Kogure, M., Yue, J., Nakamura, T., Hoffmann, L., Vadas, S. L., Tomikawa, Y., et al. (2020). First direct observational evidence for secondary gravity waves generated by mountain waves over the Andes. *Geophysical Research Letters*, *47*(17), e2020GL088845. https://doi.org/10.1029/2020GL088845

Kruse, C. G., Alexander, M. J., Hoffmann, L., van Niekerk, A., Polichtchouk, I., Bacmeister, J. T., et al. (2022). Observed and modeled mountain waves from the surface to the mesosphere near the Drake Passage. *Journal of the Atmospheric Sciences*, *79*(4), 909–932. https://doi.org/10.1175/jas-d-21-0252.1

Lim, E.-P., Hendon, H. H., Butler, A. H., Thompson, D. W. J., Lawrence, Z. D., Scaife, A. A., et al. (2021). The 2019 southern hemisphere stratospheric polar vortex weakening and its impacts. *Bulletin of the American Meteorological Society*, *102*(6), E1150–E1171. https://doi.org/10.1175/BAMS-D-20-0112.1

McLandress, C., Shepherd, T. G., Polavarapu, S., & Beagley, S. R. (2012). Is missing orographic gravity wave drag near 60°S the cause of the stratospheric zonal wind biases in chemistry–climate models? *Journal of the Atmospheric Sciences*, *69*(3), 802–818. https://doi.org/10.1175/JAS-D-11-0159.1

NRLMSIS. (2023). NRLMSIS atmosphere model [Dataset]. *NASA CCMC Instant Run System*. Retrieved from https://kauai.ccmc.gsfc.nasa.gov/instantrun/nrlmsis/

Pautet, P.-D., Taylor, M. J., Fritts, D. C., Janches, D., Kaifler, N., Dörnbrack, A., & Hormaechea, J. L. (2021). Mesospheric mountain wave activity in the lee of the southern Andes. *Journal of Geophysical Research: Atmospheres*, *126*(7), e2020JD033268. https://doi.org/10.1029/2020JD033268

Plougonven, R., de la Cámara, A., Hertzog, A., & Lott, F. (2020). How does knowledge of atmospheric gravity waves guide their parameterizations? *Quarterly Journal of the Royal Meteorological Society*, *146*(728), 1529–1543. https://doi.org/10.1002/qj.3732

Preusse, P., Schroeder, S., Hoffmann, L., Ern, M., Friedl-Vallon, F., Ungermann, J., et al. (2009). New perspectives on gravity wave remote sensing by spaceborne infrared limb imaging. *Atmospheric Measurement Techniques*, *2*(1), 299–311. https://doi.org/10.5194/amt-2-299-2009

Rapp, M., Kaifler, B., Dörnbrack, A., Gisinger, S., Mixa, T., Reichert, R., et al. (2021). SOUTHTRAC-GW: An airborne field campaign to explore gravity wave dynamics at the world's strongest hotspot. *Bulletin of the American Meteorological Society*, *102*(4), E871–E893. https://doi.org/10.1175/BAMS-D-20-0034.1

Reichert, R., Kaifler, B., Kaifler, N., Dörnbrack, A., Rapp, M., & Hormaechea, J. L. (2021). High-cadence lidar observations of middle atmospheric temperature and gravity waves at the southern Andes hot spot. *Journal of Geophysical Research: Atmospheres*, *126*(22), e2021JD034683. https://doi.org/10.1029/2021JD034683

Sato, K., Tateno, S., Watanabe, S., & Kawatani, Y. (2012). Gravity wave characteristics in the southern hemisphere revealed by a high-resolution middle-atmosphere general circulation model. *Journal of the Atmospheric Sciences*, *69*(4), 1378–1396. https://doi.org/10.1175/JAS-D-11-0101.1

Smith, R. B., Nugent, A. D., Kruse, C. G., Fritts, D. C., Doyle, J. D., Eckermann, S. D., et al. (2016). Stratospheric gravity wave fluxes and scales during DEEPWAVE. *Journal of the Atmospheric Sciences*, *73*(7), 2851–2869. https://doi.org/10.1175/JAS-D-15-0324.1

Smith, S., Baumgardner, J., & Mendillo, M. (2009). Evidence of mesospheric gravity-waves generated by orographic forcing in the troposphere. *Geophysical Research Letters*, *36*(8). https://doi.org/10.1029/2008GL036936

Stober, G., Janches, D., Matthias, V., Fritts, D., Marino, J., Moffat-Griffin, T., et al. (2021). Seasonal evolution of winds, atmospheric tides, and Reynolds stress components in the southern hemisphere mesosphere–lower thermosphere in 2019. *Annales Geophysicae*, *39*(1), 1–29. https://doi.org/10.5194/angeo-39-1-2021